GEODAR Data and the Flow Regimes of Snow Avalanches

A. Köhler,[1,2] J. N. McElwaine,[2] B. Sovilla[1]

Corresponding author: A. Köhler, WSL Institute for Snow and Avalanche Research SLF, Flüelastrasse 11, Davos Dorf, CH-7260, Switzerland, (koehler@slf.ch).

[1]WSL Institute for Snow and Avalanche

Research SLF, Flüelastrasse 11, Davos Dorf,

CH-7260, Switzerland.

[2]Department of Earth Sciences, Durham

University, Science Labs, Durham,

DH1 3LE, UK.

Abstract.   GEODAR, a custom radar system, images avalanches over the entire slope with high spatial and temporal resolution at the experimental test-site Vallée de la Sionne in Switzerland. Between winter seasons 2009/10 and 2014/15, data has been acquired from 77 avalanches. These data sets describe a wide variety of avalanches, which we classify in terms of seven flow regimes and combinations thereof. These flow regimes expand on previous classifications, with four identifiable dense flow regimes (where interaction between granules and with the flow bed dominates dynamics) and two different dilute flow regimes (where interaction between snow particles and the air becomes dominant). There is a further regime identified where snow balls simply roll down the mountain.

A cold dense regime and a warm shear regime behave like non-cohesive granular flows with velocity shear throughout the flow. A sliding slab regime and a warm plug regime occur when cohesion dominates and causes the flow units to act as solid-like objects sliding on a thin shear zone. An intermittent regime connects the cold dense regime with the suspension regime, and is characterised by highly fluctuating density and surging activity. GEODAR enables localization of these flow regimes and transitions between them in time and space. We discuss flow regime transitions in terms of snow properties, topography, speed and size of the avalanches.

This paper also serves as a reference for the data set which is made publicly available and should prove to be an invaluable resource for the development of physically based avalanche models.

Keypoints:

- Snow avalanches exhibit three different stopping mechanisms and these are primarily controlled by snow temperature

- GEODAR data are used to identify seven flow regimes which are tracked in time and space

- Many avalanches contain multiple flow regimes and transitions between these regimes are common

1. Introduction

Snow avalanches are a major natural hazard in mountainous regions both for people and infrastructure. Large and catastrophic avalanches can reach inhabited areas and their danger potential is managed with land-use planning like hazard maps, temporary measures like road closures, or permanent structures like dams. To successfully design and apply these measures, a quantitative model of the avalanche flow dynamics is essential for prediction of potential runout, impact forces on structures and the flow around dams.

It has long been known that avalanches can exhibit very different flow behaviour (Fig. 1), which has led to multiple avalanche classification schemes, *e.g. Gauer et al.* [2008], *De Quervain et al.* [1973]. In the early stages of avalanche dynamics research, airborne and dense avalanches were differentiated [*Voellmy*, 1955]. The movement of airborne avalanches is controlled by the interaction of particles with air as the flow density is usually low and particles are not in close contact to each other [*Hopfinger*, 1983]. Dense avalanches were further divided into dry and wet avalanches, and the international avalanche classification scheme [*UNESCO*, 1981] emphasises the influence of liquid water content. Dry dense avalanches act approximately as non-cohesive granular flows, whereas in wet avalanches the cohesion plays an important role and generally causes the mobility to decrease, leading to shorter runouts [*Issler*, 2003].

Here, we emphasise the importance of the snow temperature by classifying regions of avalanches as cold or warm. Indeed, *Steinkogler et al.* [2015a] showed recently with small-scale granulation experiments in a rotating drum that there is a sharp transition at around $-1\,°C$. Below this temperature individual snow grains keep their identity, but above it the

grains rapidly agglomerate into large rounded clumps. This sharp increase in cohesion and therefore in the average particle size by upto two orders of magnitude is very important for the dynamic behaviour of avalanches [*Steinkogler et al.*, 2014]. *Naaim et al.* [2013] draws a similar conclusion by analysing many large avalanches in combination with snow cover modelling, finding a temperature dependence of the effective friction.

The study of the deposits from large avalanches shows that they are often of *mixed* type [*Issler*, 2003]. *Mixed* avalanches are defined as avalanches containing a dense flowing part and a more dilute region (light-flow in *Schaerer and Salway* [1980], saltation layer in *Issler* [1998]) under a turbulent suspension or powder cloud. Deposits of avalanches also reveal that the dilute regions usually travel much farther than the denser parts, which supports the theory that mixed avalanches are not only made of layers which feed each other, but that these regions can also separate from each other [*Gauer et al.*, 2008]. *Sovilla et al.* [2015] enhanced the understanding by including a comprehensive set of dynamic data (flow height, pressure, density and velocity) into the typical structure of powder snow avalanches (PSA) [*Turnbull and Bartelt*, 2003], and characterised the above-mentioned regions as dense core, intermittent frontal region and dilute suspension region. The dense core can be further divided into the main body and the tail, and the dilute region into an energetic turbulent suspension, which is fed by the intermittent frontal region, and a decaying powder cloud, where the density and turbulent intensity are decreasing.

In this paper, we use the radar system GEODAR [*Keylock et al.*, 2014] to investigate the denser flow processes that are optically obscured under the powder cloud. The radar gives reflectivity data in high spatial (0.75 m) and temporal (111 Hz) resolution. A moving target identification (MTI) processing is applied to the data to remove the non-moving

background clutter. We call the characteristic patterns in MTI images caused by flow structures and by the interaction of the flow with the terrain *MTI signatures*. These can advect with the flow, *i.e.* streaks and lines, or can be induced by local topography, *i.e.* light and dark spots.

We are able to differentiate between starting, flowing and stopping signatures. The appearance of typical combinations of signatures is connected to the form of movement. Based on that, we characterise the dynamical processes which control the mobility of snow avalanches into different flow regimes and discuss their development in time and space.

The aim of this paper is to improve and extend previous classifications of avalanche flow regimes by using GEODAR data and other measurements, and to provide a classification that is based on the physical processes that are dominant in different regions. In this paper we define a *region* of an avalanche as a connected volume in space in which the same physical processes are dominant. Groups of physical processes in one region are then defined as *flow regimes*.

The structure of this paper is as follows. In section 2 we explain the different measurement systems and procedures used to generate the raw data and we provide a summary of all the observed avalanches and what data are available. In section 3 we present the avalanche data in detail. We describe typical MTI starting and flowing signatures and identify three different stopping signatures. We connect these with snow-cover properties, flow height and flow velocities. These results lead in section 4 to the definition of seven flow regimes, and in section 5 we give four full scale avalanche examples to show the occurrence of multiple flow regimes within each event. Transitions between flow regimes are discussed in section 6. Section 7 give a brief conclusion of the paper. Appendix A

lists all acronyms used in the text. Appendix B gives the details of the GEODAR data repository, where documentation of the different versions of GEODAR and more detailed information on radar data processing can be found.

2. Methods and data

2.1. Vallée de la Sionne (VdlS) avalanche test-site

The Vallée de la Sionne (VdlS) avalanche test-site is situated in western Switzerland, in Canton Valais [*Ammann*, 1999]. The avalanche path faces south-east and extends between the mountains peaks of Pra Roua and Crêta Besse (Fig. 2). The release area is approximately 1500 m wide and the total vertical drop is 1200 m. In the lower section, the path is channelled into two prominent couloirs. Only the left couloir is instrumented, therefore, avalanches releasing from Pra Roua (PRA) towards Crêta Besse (CB1 & CB1/2) provide the widest variety of data, whereas avalanches flowing down Crêta Besse (CB2) are observed only by GEODAR.

The GEODAR system and two cameras are situated 40 m up the counter slope in a concrete bunker facing the avalanche path. In the avalanche runout, a 20 m high steel pylon is instrumented with sensors at various heights which measure velocity, flow heights, impact pressures, temperatures and densities [*Sovilla et al.*, 2013]. Seismic sensors situated in Cavern B and Cavern A capture the ground motion caused by avalanche activity and trigger the data acquisition. Three Frequency Modulated Continuous Wave (FMCW) radars are installed in the caverns and close to the pylon [*Gubler and Hiller*, 1984], and are used to extract the flow depth and evaluate the avalanche trajectory. A weather station located close to the avalanche release zone (VDS2) and one at the deposition zone

(VDS3) provide information to reconstruct the snow cover conditions along the avalanche path (sec. 2.4).

2.2. GEODAR

The GEODAR system (GEOphysical flow dynamics using pulsed Doppler radAR) was developed by an international consortium [*Brennan et al.*, 2009] and has been in operation in VdlS since the winter 2010/11. The GEODAR system hardware and software have undergone continuous improvement. GEODAR I, II and III built upon the original design [*Ash et al.*, 2010]. GEODAR IV was a complete redesign [*Ash et al.*, 2015; *Tanha et al.*, 2017] which unfortunately suffered severely from electronic noise. GEODAR V uses the original hardware but with a different antenna system. Data presented in this paper have been obtained using the first three systems, and each of them is described in detail in the documentation of the data repository (Appendix B).

The radar parameters define the resolution in space and time: the chirp bandwidth of 200 MHz, chirp length 4 ms and sampling frequency 2 MHz give a range resolution of 0.75 m, a repetition rate of 111 Hz and a maximum range of 3 km (GEODAR III). The base-band frequency is 5.3 GHz, and the corresponding wave length of around 57 mm is roughly the minimal object size providing reflection. Therefore, GEODAR only sees the denser flow structures below the dilute powder cloud [*Köhler et al.*, 2016]. A key feature of GEODAR is that it records the full chirp signal as a raw time-domain signal. After the data have been acquired the signal can be analysed in various ways so that improved algorithm design can increase the utility of previously captured data. An important step in the processing chain is the application of a moving target identification (MTI) filter. Such filtering is used to suppress the static background signal and enhance different details

of the moving avalanche. Here, we use a FIR filter with a normalised cutoff frequency of 0.12 and normalise the output for each channel at each range before averaging across all antenna. The signal processing details are described in the data repository documentation (Appendix B).

Typically, the MTI data are displayed in range-time plots, where the radar is at range 0 m, and the MTI intensities are colour-coded (*e.g.* Fig. 3). The MTI intensities in decibels are related to the reflective area, called the radar cross section. Zero intensity corresponds to the background signal. Positive values quantify the reflection properties of the flow surface and dielectric changes throughout the flow height [*Köhler et al.*, 2016]. The avalanche front gives normally the strongest signal and it appears as a strong step change in the range-time diagram. Many internal avalanche details appear behind the front. Since these internal details are often very faint features, manual extraction and interpretation are necessary. This introduces a certain subjectivity in the results. The error is rather small for the extraction of the front and the back-edge or for highly-visible internal surges. But the recognition of certain MTI signatures relies to a certain extent on expertise. The detailed description of MTI signatures in section 3.1 provides a classification to make such analyses more consistent between different users. We define *MTI flowing signatures* as those within the flow path, and *MTI stopping signatures* as those near where the avalanche stops.

2.3. Release location, avalanche trajectory, front velocity

The release location for each avalanche event was estimated by using four different data sources, namely pictures, FMCW radars, seismic sensors and the GEODAR. Pictures of the slope were taken every half an hour. If the full avalanche is visible in the images, we

applied a geo-referencing scheme to get the full outline and defined the release location as the point of highest elevation [*Köhler et al.*, 2016]. For avalanches that occurred during snowfall or periods of cloudy weather (typically PSA), the release location could not be determined from pictures alone. In this case, the FMCW radars and seismic instruments in Cavern B and Cavern A indicate whether the flow went over them and thus determine the favoured couloir followed by the avalanche and the most probable release location. Further, the GEODAR image includes characteristic shadow spots which correspond to specific shaded areas in the terrain (Fig. 2), and can be used as a terrain orientation.

Knowledge of the avalanche trajectory is crucial to obtain the ground-parallel velocity, since the radar beam hits the terrain surface at a particular line-of-sight angle. We define the 1D avalanche thalweg as the line of steepest descent starting from the release location. The procedure to project the range and time data from the front along this thalweg, that is to gain the trajectory s and the ground-parallel front velocity $\dot{s}$, is described in detail in *Köhler et al.* [2016]. Throughout the paper distances are referring to range from the bunker rather than arc-length, since the start of an avalanche is often missed due to a delayed trigger.

Even if the release location is not known precisely, the line of steepest descent from a certain region converges quickly to a common thalweg. So for the GEODAR data it is sufficient to know roughly the release region to estimate the ground-parallel velocity in the lower part of the path. In this case, we define the release coordinates [N, E, Z in m] manually for each region in the Swiss coordinate system CH1903 (SRID 21781): PRA [127425, 593311, 2491], CB1 [127663, 593265, 2582], CB1/2 [127930, 593378, 2586] and CB2 [128331, 593540, 2656] (Fig. 2).

2.4. Snow properties

Snow cover properties have a large influence on the avalanche dynamics [*Steinkogler et al.*, 2014]. In particular, the snow temperature and the liquid water content are crucial properties which cause different rheological behaviour of the flowing snow [*Naaim et al.*, 2013; *Steinkogler et al.*, 2015a].

Unfortunately, very few manual snow profiles are available for the avalanches in our data archive since most of them occurred naturally and the path was rarely accessible immediately after the events. To overcome this problem, we used the numerical model SNOWPACK [*Lehning et al.*, 2002] to reconstruct the snow properties for each avalanche event. The data from two automatic weather stations were used as the input for the simulations. The weather station VDS2 (2390 m a.s.l.) was used as a proxy for the snow conditions in the release areas, and the weather station VDS3, close to the pylon at 1680 m a.s.l., was used to reconstruct the snow cover in the deposition area (Fig. 2).

The calculated snow properties must be taken with care. In particular, the modelled snow cover will be different from the actual conditions in the flow path since former avalanche activity and entrainment/deposition can alter the old snow cover significantly. However, the SNOWPACK model accounts for energy fluxes within the snow cover through the ground and the atmospheric boundary. The meteo data parameterising the atmospheric boundary are more important for simulations of new snow precipitation and its metamorphism rather than influences from the old snow cover underneath. Additional uncertainty arise as the simulations were performed on meteo data from flat-field measurements, and incoming global radiation is expected to be different compared to the east-facing slopes of Vallée de la Sionne. This results in situations with typical spring con-

ditions, *e.g.* diurnal melt-freeze cycles, in a delayed warming in the simulation compared to expected warming in the avalanche path.

As a first approximation, we define the uppermost $0.5\,\mathrm{m}$ of the snowpack to be representative for the snow properties of the flowing avalanche. Snow properties are averaged over this depth and the simulated snow temperature, liquid water content [*Wever et al.*, 2014] and new snow sum are summarized for each avalanche in Table 1 for the lower ($_b$) and upper ($_t$) weather stations. We have manually chosen the relevant time window up to six days before each avalanche to estimate the sum of new snow precipitation.

2.5. Flow heights

Avalanche flow heights for the cold avalanches in our data archive are derived from FMCW measurements performed in Cavern B [*Gubler and Hiller*, 1984]. FMCW radars operate like ground penetrating radar but point up through the flowing snow rather than downwards to the ground. Due to large attenuation of the electromagnetic signal by liquid water content, the radars have limited usefulness in wet snow conditions or if large snow deposits cover the radar. For nearly all warm flow avalanches no flow height information from FMCW can be obtained.

The interpretation of the FMCW radar signal is not straightforward since the signal is influenced by multiple reflections of layers in the snowpack [*Schmid et al.*, 2014], and the depth accuracy is dependent on the unknown density of the snow pack as well as the flowing snow. Nevertheless the FMCW radar gives a detailed but qualitative picture of the flowing avalanche including entrainment, deposition, flow height changes, wave heights and flow structure [*Sovilla et al.*, 2006]. Flow heights of surges and waves were manually

extracted and connected to the surge flowing signatures in the GEODAR data [*Köhler et al.*, 2016].

2.6. Avalanche cadastre

Since the initial deployment in December 2010 until May 2015, the GEODAR system has measured 77 avalanche events, summarized in Table 1. Each avalanche is identified by the archive number (`SLF-Nr`) which is the hydrological season followed by a four digit running number. The GEODAR data are identified by the trigger timestamp in the date format year-month-day-hour-minute-second. Most of the avalanches were naturally released and only few were artificially released during an experiment. Artificially released avalanches are marked with an asterisk in the SLF-Nr in Table 1.

The first part of the table contains metadata and information directly derived from the GEODAR measurements. The release area and altitude are derived as described in section 2.3, and the runout length is defined as the smallest radar range reached by the avalanche [*Pérez-Guillén et al.*, 2015]. The column `stop` characterises the stopping signatures visually identified from the GEODAR plots: (A) starving, (B) backward propagating shock and (C) abrupt stopping (sec. 3.2). For some events a combination of two stopping signatures exists. In such case, we have indicated this by mentioning the main and a sub-signature. For avalanches which stopped above a range of $1800\,\text{m}$ (sluff avalanche size) or stopped in the valley floor (very large), no stopping signature could be inferred (-). We also average the slope angle over the last $100\,\text{m}$ (range) of the trajectory before the avalanche stops, and give the velocity v_s at $100\,\text{m}$ in range before the stopping point. This is an arbitrary distance which we chose since we have this data for a

large number of avalanches and it gives a robust measure of the avalanche speed and the following deceleration.

Pictures prior to and after the event (`Img`) are number coded regarding their information content: (0) no images, (1) deposit visible as lower path outline, (2) full outline. Availability of FMCW data in Cavern A and B (column `A` and `B`) is coded with the following criteria: (1) avalanche signal, (0) no avalanche signal, (-) missing signal due to wet snow interference. Column `C` indicates the availability of pylon measurements.

The last part of Table 1 contains information on the snow cover derived from snowpack simulations as described in section 2.4. The fields TS_b, TS_t, LWC_b and LWC_b are the mean snow cover temperatures and the liquid water content at the bottom $_b$ (VDS3) and top $_t$ (VDS2) weather stations, and refer to the average of the uppermost $50\,\mathrm{cm}$ of the snow cover. HN_b and HN_t are the sum of new snow precipitation in up to 6 days prior to the avalanches at the bottom and top stations, respectively.

3. Results

Snow avalanches are geophysical flows with diverse flow behaviours of which some of them are shown in the pictures in Figure 1, and with different composition of *flow units*[1] from fine grained to rounded granules to large clusters as shown by *Ancey* [2007]. The GEODAR radar enables to observe this wide diversity even in weather condition of low visibility and — more important — through a opaque powder cloud. Differences can be observed in the radar signatures of the internal flow structures and in particular in the stopping signatures, which we categorised into three types. We also present data on flow velocities, snow properties and flow height where this is available.

For naturally released avalanches the GEODAR system is triggered seismically from geophones in Caverns A and B, so, generally we miss the initial release and early stages of the flow. For artificially released avalanches this problem does not arise and in addition sometimes a sequence of multiple avalanche releases only a few minutes apart could be captured.

3.1. MTI flowing signatures

Figure 3 is a collection of GEODAR flowing signatures which frequently occur in our data. The upper row shows streak signatures which move with the flow, and the lower row shows internal signatures which are fixed relative to the topography. We discuss them in more detail in section 4 when connecting them with flow regimes.

The GEODAR images show most clearly the front (Fig. 3A) and the tail of an avalanche. Inside the avalanche, where the flow is steady, the signature is homogeneously coloured (Fig. 3A). If, instead, internal structures in the flow exist, they become visible because they are in general a sequence of darker and light MTI intensities.

The most obvious flowing signatures in the MTI are dark streaks [*Vriend et al.*, 2013], whose steepness give the flow velocity towards the radar. *Köhler et al.* [2016] connected these streaks to internal surges, which are denser and give stronger reflections than the surrounding flow. These surges can have long trajectories and appear throughout the full avalanche (Fig. 3B), or they can have short trajectories and exist only in the proximity of the avalanche front (Fig. 3C).

Fig. 3B shows an example of long trajectory surges. These surges can be generated when the topography splits the avalanche into several arms, in which case we call them separate fronts (Fig. 1A). Or they can originate from secondary slab releases and move

along the same thalweg in which case we call them major surges [*Köhler et al.*, 2016]. In both cases, they can be regarded as individual avalanches with independent flow dynamics and flow regimes [*Köhler et al.*, 2016].

Fig. 3C shows an example of short trajectory surges. These minor surges only occur in fully developed powder snow avalanches. As long as they are behind the front, they can have velocities larger than the front velocity and thus, they have a large influence on the front dynamics and avalanche mobility due to overrunning [*Köhler et al.*, 2016].

Fig. 3D shows an example of streaks often present in very slow avalanches. These streaks are running parallel to the front and are probably the result of flow units which change their structure only little during motion. Figure 1C shows an example picture of such solid-like flow units, which did not interact with each other. Often completely blank spots are visible together with this parallel streak signature (Fig. 3D). These blank spots can have zero intensity even when the surrounding signal can be very strong. The location of these blank spots depends on the frequency response of the MTI filter. They may occur when the flow surface is smooth so that there is no change in reflected amplitude from one chirp to another, or in cases where the variations are narrow band are filtered out by the MTI filter.

Beside streaks which are located inside the avalanche, we can identify single line features often starting from the main deposit or running in front of the avalanche as shown in Fig. 3E. Comparison with videos and photos of the debris reveal that these are traces of single snow balls or snow-wheels (Fig. 1B). These have been observed to roll down the slope for as far as one kilometre (Fig. 7 or in 1D).

Some types of flowing signatures always occur in the same place on the slope and do not advect with the avalanche flow, so that it is strongly suggestive that they are triggered by certain topographic features. They can be areas of greater or lesser variation in reflected signal corresponding to darker or lighter signatures in the MTI plots. Fig. 3F shows an example of a light spot typically observed in avalanches from the PRA release area. The location of the spot corresponds to a shaded area, which is not reached by the GEODAR beam because of topographic obstructions (Fig. 2). Figure 1A shows the corresponding picture of this avalanche: The suspension cloud overtops the small gully (black circle) while the denser parts are shaded from the radar. These spots can be used as a reference to trace the avalanche trajectory, and to estimate an upper limit of the flow height of denser material below the suspension cloud.

Fig. 3G shows an example of a darker region. This one is located at $1350\,\text{m}$ to $1450\,\text{m}$ and corresponds to the steep entrance of the couloir. The dark spot indicates an increase in radar cross section [*Salm and Gubler*, 1985]. In steep terrain, the avalanche head may become more turbulent or fluidize and may exhibits a larger area causing reflections of the signal.

Fig. 3H shows that avalanches may contain structures which leave a triangular outline in the MTI plots. Here, the avalanche consists of four surges of which three trigger a triangular signature beginning at the same range. While the upper boundary is connected to a certain location, the lower boundary moves upward with time. These are presumably standing shocks or jets triggered by topography. This particular avalanche has been described with flow height and velocity data in *Köhler et al.* [2016].

Fig. 3I shows that the flowing signature can change locally and may indicate an abrupt change of the flow properties. This panel shows further that almost any radar image contains horizontal bands (*e.g.* see Figure 7 to 10). When they exist through the full recording length or are outside the avalanche area, they belong to noise from electronic or environmental sources like waving trees in the wind (Fig. 10). But such horizontal bands can also appear inside avalanches, and may result from interaction with topography.

Finally, for a few avalanches we have captured the release of the snow slab as Figure 1E shows. It is possible to observe the complete slab starting simultaneously and leaving a vertical starting signature in the MTI plot. While in the beginning some streaks may indicate the movement of large snow blocks, with time the signature becomes homogeneous as the blocks fragment to small grains (*e.g.* Fig 3J). Point release avalanches would give a different MTI starting signature (Fig. 9C) but we have little data on this, presumably because we miss the start of the vast majority of avalanches.

3.2. MTI stopping signatures

The stopping phase of an avalanche is nearly always recorded by the GEODAR system. By *stopping signature* we mean the pattern which the stopping mechanism of the avalanche traces in the radar images. We identify three distinct stopping signatures in the data sets, with typical examples shown in Figure 4.

We define the corresponding stopping mechanisms as: (A) starving, (B) backward propagating shock, and (C) abrupt stopping. A further tail deposition mechanism (D), often visible at large ranges, has also been included. The stopping signatures (A–C) were manually assigned to each avalanche event, and summarized in Table 1 in column `stop`. In the following we describe the characteristics of each deposition mechanism.

Starving (Fig. 4A): Almost 40 % of the avalanches in the database are characterised by a progressive decrease in avalanche flowing length just before deposition. Material is deposited at the avalanche tail, while at the same time, the front continues to flow. The flowing length gradually diminishes and the front finally starves. Only a small part of the avalanche mass reaches the final runout position. This mechanism is often associated with the presence of surging in the avalanche flow [*Köhler et al.*, 2016]. The avalanche deposits are usually smooth and wide spread [*Issler*, 2003] and the deposit heights are generally lower than the flow height [*Sovilla et al.*, 2010].

Backward propagating shock (Fig. 4B): Around 20 % of the avalanches in the database are characterised by a stop of the avalanche front, followed by a progressive piling up of the incoming material. There is an upslope, or backward propagating shock clearly visible on the MTI plots. Often the shock travels with a fairly constant velocity and appears as an upward-sloping line in the MTI plots. The shock velocity is a phase and not a group velocity: only the shock wave and no material travels upward [*Köhler et al.*, 2016]. Typically the deposits of these flows are rough and granular, but they have little large scale structure above the size of the snow particles or blocks.

Abrupt stopping (Fig. 4C): Around 30 % of the avalanches in the database are characterised by an abrupt and almost instantaneous stop throughout the complete flow length. This stopping mechanism is characterised by a vertical signature in the MTI plots. The signal is often characterised by streaks which run parallel to the avalanche front and avalanche tail, suggesting that the avalanche velocity is constant over large parts of the flow. Typically, these flows are laterally confined by levées or icy shear planes and the deposits are often rough with steep and sharp boundaries [*Issler*, 2003]. For around 30 %

of these avalanches, the dominant abrupt stopping mechanism coexists with the backward propagating shock mechanism, *e.g.* Figure 7C and at 1000 m in Figure 8.

Tail deposition (Fig. 4D): Snow deposition can occur not only in the avalanche runout zone but also along the avalanche path when the slope angle is smaller than around 30 degrees [*Sovilla et al.*, 2010]. Indeed, at higher altitudes the MTI plots are often characterised by a gradual decrease in MTI intensity towards the tail. Such a signature is consistent with a progressive decrease in flow depth which can be caused by both loss of material at the avalanche base or by the avalanche elongation and consequent retention of material at the avalanche tail [*Sovilla et al.*, 2010].

3.3. Snow properties and flow velocity in the stopping phase

In Figure 5, we connect each stopping mechanism with the snow temperature (left), the liquid water content (middle) and give the distribution of front velocity v_s corresponding to the velocity at 100 m in range before the avalanches stop (right).

The starving deposition mechanism (Fig. 4A) is a specific feature of cold avalanches, *i.e.* avalanches with average snow temperature below $-1\,°C$. At these temperatures snow has a low ability to sinter and to form granules, and fragmentation is more important than aggregation [*Steinkogler et al.*, 2015a]. The avalanche composition is mostly fine grained material and some fragments of released slabs and entrained snow.

In contrast, the backward propagating shock (Fig. 4B) is characteristic for avalanches with average snow temperatures close to zero degrees, at least in the deposition zone (Fig. 5). For the liquid water content our data are inconclusive due to a large variation between 0.2 % and 3 % caused by only seven data points in the box plots, but greater than for the starving deposition mechanism. For these snow cover characteristics we

believe that aggregation of snow crystals exceeds fragmentation and may give rise to the formation of persistent-moist granules [*Steinkogler et al.*, 2015a]. However, this stopping mechanism can also occur in dry granular flows [*Gray et al.*, 2003], if they encounter a sharp reduction in slope angle or increased surface roughness such as pre-existing debris, so we also expect this on occasion for cold snow.

For avalanches with an abrupt stopping signature (Fig. 4C), the conditions for cohesion leading to the formation of persistent-wet granules [*Steinkogler et al.*, 2015a] prevail for snow temperatures reaching $0\,°\mathrm{C}$ and LWC above $1.8\,\%$.

The front velocities v_s (Fig. 5, right) give a measure of the avalanche deceleration during the last $100\,\mathrm{m}$ in relation to each stopping mechanism. Avalanches characterised by a starving stopping mechanism are the fastest with up to $30\,\mathrm{m\,s^{-1}}$ (blue). Note that the largest avalanches reaching the valley bottom had to be excluded from this analysis since their stopping could not be observed, so that the distribution is biased towards smaller velocities.

In contrast, avalanches characterised by abrupt stopping are the slowest with even large avalanches having velocities of only up to $5\,\mathrm{m\,s^{-1}}$ (red). The few higher velocities belong to medium sized avalanches which present a mix between abrupt and backward propagating shock stopping mechanisms and for which the abrupt stopping signature appear shortly before stopping. They are indicated with "C/B" in Table 1, and bias the velocity distribution towards higher values.

The velocities of avalanches characterised by the backward propagating shock mechanism are in between these extremes. Most of them have a flow velocity of around $10\,\mathrm{m\,s^{-1}}$ to $20\,\mathrm{m\,s^{-1}}$ (yellow).

Given that the avalanches have different sizes and stop at different locations along the path, it is in general complicated to compare the velocities directly, and leading to greater error in the velocity distribution. Even with this uncertainty, the velocity data shows clearly a trend between the three stopping signatures (Fig. 5).

3.4. Flow height and velocity of cold avalanches

Avalanches characterised by the starving stopping mechanism give a broad distribution of velocities v_s (Fig. 5, right), since they can cover a large range of runouts (Tab. 1). We investigate their flow characteristics in more detail at the location of Cavern B.

We extracted the flow heights of the front and consecutive surges from the FMCW profiling radar, and related them to the corresponding flow velocities from the MTI plots at Cavern B (Fig. 6). Round and square symbols indicate the amount of new snow and avalanche size, respectively. A star indicates secondary avalanches which happen after previous avalanche activity and thus find different flow bed conditions in their path. We have identified three different clusters highlighted with blue, yellow and green circles. Interestingly, we did not record any primary avalanche with flow heights in between the blue and yellow clusters, even so the velocity between both clusters is smooth.

The Froude number is defined as $Fr = \dot{s}/\sqrt{gh\cos\theta}$ and gives a measure of whether the flow is super-critical or sub-critical (black dashed lines in Fig 6). All cold avalanches have Froude numbers Fr between 3 and 8, and from a hydrodynamic point of view, their flow is super-critical and their motion is most likely turbulent or fluidized [*Issler*, 2003]. There is a little trend to higher Fr with avalanche size and amount of new snow precipitation.

The **blue cluster** contains large avalanches which happened after significant snow fall events with precipitation of more than 70 cm new snow. All large avalanches in this cluster

reached the valley bottom. The flow heights were between 5 m and 8 m, and the velocities were as high as $30 \, \text{m s}^{-1}$ to $55 \, \text{m s}^{-1}$. Minor surges are found in the blue cluster as well.

The **yellow cluster** contains small to medium sized avalanches which starved shortly below Cavern B or at the end of the couloir. Previous snowfall gave mostly not more than 30 cm of new snow. The flow heights were limited to around 3 m, and the velocities did not exceed $25 \, \text{m s}^{-1}$. Additionally, some second surges appear in the yellow cluster and indicate the dense core and dense tail region of larger avalanches [*Sovilla et al.*, 2015].

The **green cluster** contains secondary avalanches, that followed a reasonably large previous event in the same path, *e.g.* #15-0017 and #15-0019 were released shortly after #15-0016. The snow cover was therefore altered, and the avalanches found less fresh snow but only harder deposits to entrain. These avalanches had high velocities between $25 \, \text{m s}^{-1}$ and $40 \, \text{m s}^{-1}$, but relatively low flow heights up to 4 m. The Froude number was highest for these avalanches. Some internal surges appear in the green cluster as well.

4. Avalanche flow regimes

The GEODAR plots of avalanches at the Vallée de la Sionne can exhibit a large variety of MTI flowing and stopping signatures as described in the previous section 3. By combining these signatures with the snow cover conditions at the moment of the event, we identify seven different flow regimes. The MTI flowing signatures are not always enough to uniquely classify each regime, but in conjunction with the MTI starting and stopping signature each regime can be unambiguously identified. For example, the warm shear and the cold dense regime do not differ much in the MTI flowing signature, both are homogeneous and can have similar velocities, but the stopping signature and the snow

temperature data separate both regimes. We will not discuss glide snow or slush flow regimes as these have not occurred in our data from Vallée de la Sionne.

In the following we will give a short definition for each of the flow regimes and we will link them to the MTI signatures and snow cover properties. In section 5 we will show that avalanches are made of a combination of different flow regimes, and finally we will discuss in section 6 how transitions between flow regime may occur.

4.1. Warm Shear Regime (WSR)

The primary indicator for this flow regime is the MTI stopping signature, a backward propagating shock (Fig. 4B). This occurs for snow temperatures slightly below zero and liquid water content may play a role (Fig. 5). For these snow characteristics, it was shown by *Steinkogler et al.* [2015a] that aggregation exceeds fragmentation and should give rise to the formation of persistent-moist granules. These granules can have a diameter of several decimetres [*Bartelt and McArdell*, 2009]. The deposition due to piling up of material and the relatively high velocities reached by these flows, up to $\approx 25\,\mathrm{m\,s^{-1}}$, suggest that the cohesive forces acting between granules are not sufficient to glue particles together into larger units. They may flow as a visco-plastic material with kinetic stresses above the yield strength and shearing is possible. The MTI flowing signature is homogeneous (Fig. 3A), further suggesting that the flow is fluid-like rather than solid-like, that is, it is sheared throughout its depth so that the surface is steadily changing. We define this flow regime as *warm shear regime* (WSR).

4.2. Warm Plug Regime (WPR)

This flow regime occurs when the snow cover temperature is isothermal, $T = 0\,°C$, with a median liquid water content of $1.8\,\%$ (Fig. 5). These snow cover characteristics are an indication of the formation of large persistent-wet granules [*Steinkogler et al.*, 2015a]. The MTI flowing signature reveals parallel streaks (Fig. 3E), probably corresponding to large granules or surface undulations which are transported at the avalanche surface over large distances, indicating very little mixing during the flow, that is the surface is a pseudo-plug. Blank spots in the MTI images may belong to parts of the flow where the surface is smooth. The velocity is typically less than $10\,\mathrm{m\,s^{-1}}$ (Fig. 5). Since the velocities are relatively low and cohesion between granules is large, they can easily stick together and give rise to large flow units which behave like gliding, solid-like blocks [*Issler*, 2003]. These are most likely flowing as a visco-plastic fluid with a large pseudo-plug region and usually stop abruptly (Fig. 4C). The MTI data suggest that these blocks can be upto $100\,\mathrm{m}$ long (Fig. 8D). Deposit investigations and pictures confirm these large flow units and highlight the presence of a former granular structure, shear planes, gliding surfaces and levées (Fig 1C). We define this flow regime as *warm plug regime* (WPR).

4.3. Intermittent Regime (IR)

In the frontal region of a fully developed powder snow avalanche, the MTI flowing signature is characterised by short streaks lasting a few seconds, which indicate an intense surging activity (Fig. 3C). These minor surges can flow up to $50\,\%$ faster than the avalanche front. Once the internal surges reach the front they quickly decelerate and starve giving the front an intermittent character [*Köhler et al.*, 2016]. The typical MTI stopping signature of these regions is characterised by multiple surges at the front and starving at the tail (Fig. 4A). For this regime, snow temperature is always below $-2\,°C$,

thus, granulation does not occur or is rather limited, and fragmentation of released and entrained snow cover gives rise to fine grained material. Further characteristics of this flow regime are flow heights up to 9 m with velocities as high as $60\,\mathrm{m\,s^{-1}}$ (blue cluster in Figure 6). We define this flow regime as *intermittent regime* (IR) and it was described in detail in *Sovilla et al.* [2015].

4.4. Cold Dense Regime (CDR)

Not all cold avalanches develop an intermittent regime. These cold avalanches do not exceed a flow height of 4 m and have a velocity below $30\,\mathrm{m\,s^{-1}}$ (Fig. 6). Similar to those with the intermittent regime they are characterised by the starving stopping mechanism. We expect that given the right topography, *e.g.* a concave path or a strong increase in roughness, these flows may also stop with a backward propagating shock [*Gray et al.*, 2003]. These flows are often concentrated in a single surge. Such a single surge gives a homogeneous MTI flowing signature and does not exhibit internal line features (Fig. 3B). We speculate that these avalanches consist of grains in solid contact behaving like a dry granular flow with negligible influence from the air. We define this flow regime as *cold dense regime* (CDR).

In several CDR flows, MTI plots show triangular shaped features at specific ranges (Fig. 3H). We interpret these features as standing waves or shocks [*Gray et al.*, 2003; *Faug et al.*, 2015] or even jets [*Hákonardóttir et al.*, 2003], perhaps initiated by obstructions and terrain features such as changing roughness, slope [*Hopfinger*, 1983] or narrowing width of the couloir. Standing shocks occur when the flow is super-critical, that is the Froude number is greater than 1, so that their existence is dependent on flow height and velocity. In avalanche both parameters are normally highest at the front and subsequently

decrease towards the tail. This could explain the triangle shape: for a fast front with large flow heights, the shock may extends a long way forward from the obstruction. And as soon as both parameters decrease, the shock moves upward and closer to the obstruction (Fig. 9A). For a jet, the downslope distance varies with the flow velocity and the launching angle, and again both parameters change over time. The launching angle depends on the inclination of the obstruction's upstream face and may change due to smoothing by the flow itself (self-ramping). If the Froude number is high enough other instabilities such as roll waves (Fig. 1B) may develop and there is some evidence for this [*Köhler et al.*, 2016].

4.5. Snowball Regime (SBR)

Avalanches containing warm snow can give rise to individual snowballs or snow-wheels rolling down the slope (Fig. 3E). They show up as individual lines with speeds of up to $20 \, \text{m} \, \text{s}^{-1}$. The snowballs usually come out of WPR or WSR regions, indicating their granular composition, but fragments in cold avalanches can also show similar behaviour (Fig. 1B). We call this regime *snowball regime* (SBR).

4.6. Sliding Slab Regime (SSR)

Most cold avalanches and occasionally warm avalanches start with a slab failure. This gives an MTI starting signature of a vertical line. The lowest point of this line can be tracked to follow the initial acceleration of the slab (Fig. 3J). The slab fractures almost instantaneously after release and each individual fragment start to slide down-slope (Fig. 1E). The fracturing process can last for up to $200 \, \text{m}$ until the avalanche consists of small snow clods [*Issler*, 2003], and transitions into a dense regime. We call this regime the *sliding slab regime* (SSR).

4.7. Suspension Regime (SR)

The GEODAR does not measure the avalanche powder cloud since the cloud consists of single snow grains at the millimetre scale. However, this flow regime can be observed with video- or photogrammetry [*Turnbull and McElwaine*, 2007] and detected with air pressure and density sensors, and is listed here for completeness. The powder cloud height is much larger than the denser parts of the flow and it accompanies the IR or sometimes an avalanche exhibiting only a CDR. While the denser parts disappear in shadow areas in the avalanche path (Fig. 2), a suspension cloud can extend well above (Fig. 1A). Since there is still some MTI intensity (Fig. 3F) , the suspension regime may transport a few larger snow clods. We call this regime the *suspension regime* (SR).

5. Avalanche examples

Avalanches at the Vallée de la Sionne are always characterised by a combination of two or more flow regimes. In order to show the most relevant flow regimes and combinations of them, we present four different avalanche examples extracted from our database. The first two examples contain mainly warm snow, whereas the later two examples contain cold or mostly cold snow.

5.1. Avalanche #12-3060: mainly warm shear

Avalanche #12-3060 naturally released in the morning of 15 March 2012 (Fig. 7). Although the avalanche release was not captured by the GEODAR, pictures show that the avalanche started as a full-depth avalanche and eroded some soil (Fig. 1D). The average snow cover temperature to 50 cm depth at the upper weather station was $-1.9\,°C$, but we

expect that the avalanche started already with warm snow because typical freezing cycles in spring conditions bias the temperature estimation (sec. 2.4).

The avalanche had developed the typical characteristics of a *warm shear regime* with an homogeneous coloured MTI plot (Fig. 7A), and no internal structures such as internal streaks close to the front as indicative of surges or roll-waves.

The example consisted of two fronts which entered the couloir at different locations (Fig. 7A). The first front entered the couloir with a velocity of around $20\,\mathrm{m\,s^{-1}}$ to $25\,\mathrm{m\,s^{-1}}$ before deceleration started at $1150\,\mathrm{m}$, bringing the first front to rest at $950\,\mathrm{m}$. The second front was captured from $1700\,\mathrm{m}$ range onward. Its velocity increased from $12\,\mathrm{m\,s^{-1}}$ to slightly over $20\,\mathrm{m\,s^{-1}}$ in the couloir. As it hit the deposits of the first front at $1200\,\mathrm{m}$ to $1300\,\mathrm{m}$, it decelerated to only $2\,\mathrm{m\,s^{-1}}$ and stopped at $1080\,\mathrm{m}$. The front velocity of avalanches in the warm shear regime is in general medium fast and react to changes in the terrain and flow path.

The snowball regime shows up as lines starting from the deposit of the first front (Fig. 7B) and continued until the valley floor (Fig. 7D). The second front showed these granules as well, but they did not travel as far (Fig. 7C). Probably they were stopped on the rough surface of the deposit from the first front. These snowballs come from already existing large granules formed earlier and show the granular composition of the WSR (Fig. 1D).

The main stopping mechanism characterising this avalanche (Fig. 7B) is the backward propagating shock (Fig. 4B). However, especially in the deposit of the second surge (Fig. 7C), the characteristics of the abrupt stopping mechanism (Fig. 4C) can be also

recognised. This suggests that the second front may already have partially evolved into a warm plug regime (WPR).

5.2. Avalanche #13-3019: from cold to warm plug

Avalanche #13-3019 naturally released on 1 February 2013 during a snow storm with a rain limit at $2000\,\text{m a.s.l}$ (Fig. 8). Although the avalanche release was not captured by the GEODAR, we expect that the avalanche started as a cold slab since the average snow cover temperature at the top weather station, in the upper $50\,\text{cm}$ of snow cover, was $-2.2\,°\text{C}$.

The GEODAR was switched on when the avalanche reached the range $1800\,\text{m}$ to $2300\,\text{m}$. The first front entered the couloir with a velocity of up to $40\,\text{m s}^{-1}$, and stopped at around $850\,\text{m}$ with the starving nose mechanism (Fig. 4A). A small intermittent regime (IR) can also be identified by the characteristic streak signature (Fig. 8A).

The warm plug regime (WPR) started at $900\,\text{m}$ (Fig. 8B), and continued until the valley floor. The average front velocity of the WPR region was only $2\,\text{m s}^{-1}$ to $3\,\text{m s}^{-1}$. The WPR can be recognised by the existence of several semi-independent flow units. Each of these visco-plastic units moved with almost uniform velocity. The picture in Figure 1C suggest that single packages are separated by levées with steep and icy shear planes [*Issler*, 2003]. Since each unit is sliding as a solid-like block, any surface unevenness moves coherently and gives rise to the characteristic MTI flowing signature of parallel streaks (Fig. 8C) or even blank spots in the MTI (Fig. 8E). All these flow units stopped with the abrupt stopping mechanism (Fig. 8D).

It is possible to recognise a region with a backward propagating stopping shock (Fig. 4B) in the avalanche tail at a range of around $1200\,\text{m}$ and time of $200\,\text{s}$, indicating that the

avalanche tail may here developed a warm shear regime. This range corresponds to an altitude below the rain limit (Fig. 2), but also to the end of the steep couloir.

5.3. Avalanche #13-3005: mainly cold dense

The avalanches in Figure 9 are examples of the cold dense regime (CDR), as the average snow temperature in the release area was $-9.8\,°C$. These small avalanches released as small slabs or as point releases (Fig. 9C), and typically started depositing at the end of the couloir. These example avalanches had a flowing length of only around 100 m. Other avalanches in the CDR can have a larger length, but it is remarkable that avalanches with such a short flowing length can maintain their movement over distances as long as 1500 m.

These CDR avalanches have a homogeneous MTI flowing signature with no internal features like streaks and they are normally characterised by a single surge. A single triangular feature exists at a range of 1480 m (Fig. 9A). The signal strength gradually decreases towards the tail (Fig. 9B). This is in agreement with the FMCW radar data from Cavern B which showed a smooth and continuous decrease in flow height between front and tail, while the maximum flow depth did not exceed 3 m to 4 m (Fig. 6).

The avalanches quickly reached a steady state velocity, where gravity was in approximate balance with the effective basal friction. Usually, the front velocity is in the range of $10\,\mathrm{m\,s^{-1}}$ to $20\,\mathrm{m\,s^{-1}}$. As the examples in Fig. 9 show, the velocity was relatively constant over a large portion of the avalanche trajectories. The front velocity was surprisingly insensitive to the slope of the terrain as there is no further acceleration at the entrance of the couloir. At one point, the avalanches started to decelerate, and stoped with the starving stopping signature (Fig. 9B).

5.4. Avalanche #14-0012: fully developed powder snow avalanche

The front of a powder snow avalanche, such as in Figure 10, appears as a straight line in the GEODAR data from shortly after the initiation to shortly before deposition. Thus the front velocity seems to be fairly independent of terrain. Note however that this front is not in general the front of the powder cloud since fine snow grains are not imaged by the the radar. Instead the signal comes from large blocks in the intermittent region or the dense core. In the example avalanche in Figure 10 the front velocity was around $35\,\mathrm{m\,s^{-1}}$ with a slight acceleration as it entered the steep couloir. It is this location where the MTI flowing signature becomes darker and streaks indicate the beginning of the IR (Fig. 10A). *Köhler et al.* [2016] defined these streaks as minor surges of the IR, which can flow with higher velocity than the front, and by overtaking it caused shooting-like movement and a discontinuous front velocity. After the passage of the IR, the MTI flowing signature becomes more homogeneous (Fig 10A) indicating the evolution of the flow towards a cold dense regime (CDR).

The MTI stopping signature at the final runout (Fig 10D) indicates starving (Fig. 4A). *Köhler et al.* [2016] suggested that a starving starts as soon as all minor surges from the IR have overtaken the front. Indeed, the GEODAR data in Fig. 4A supports this hypothesis by showing the starving of many minor surges before finally the nose stops.

Finally, a slow moving flow feature evolved at the end of the couloir (Fig. 10B), showing the typical MTI flowing signatures of the warm plug regime (Fig. 10C). This feature moved with velocities of only $1\,\mathrm{m\,s^{-1}}$ to $2\,\mathrm{m\,s^{-1}}$ and came to rest with the abrupt MTI stopping signature (Fig. 4B). Some parts of this feature also exhibited a backward propagating shock (Fig. 4C).

6. Flow regime transitions

As shown in the previous examples, a single avalanche can be characterised by multiple flow regimes. The understanding of the physical processes governing flow regime transitions is thus of fundamental importance to predict the avalanche dynamics. Particularly relevant are transitions between the main five flow regimes, namely suspension, cold dense, intermittent, warm shear and warm plug regime.

The first important transition can be observed in cold avalanches that normally starts as dense flows. Small avalanches often stay in this cold dense regime, but medium to large flows usually develop an intermittent regime (Fig. 6) and a suspension regime. The flow transition between CDR and IR typically occurs at the entrance of the couloir below 1500 m and manifests itself with the typical streak MTI flowing signature and darker spots in the MTI plots (Fig. 10). As previously discussed, the darker MTI flowing signature could be the result of rougher terrain causing increased agitation in the flow, perhaps a higher granular temperature or higher turbulent energy. The lines result from internal surges near the avalanche front [*Köhler et al.*, 2016]. The origin of the surges is not completely clear yet, but since they occur as soon as the avalanche reaches a certain size and speed this suggests that they are a flow instability such as roll-waves. Figure 6 suggests that surges build above a velocity of $20\,\mathrm{m\,s^{-1}}$ to $30\,\mathrm{m\,s^{-1}}$. This is in accordance with the findings of *Gauer et al.* [2008] that the effective friction, in their words the retarding acceleration, changes at similar velocities. The surges have a life time of a few seconds and the longitudinal extent of the IR is usually up to a couple of hundred metres.

The second relevant flow transition observable in our data set occurs in warm avalanches and manifests itself as a change from a shear regime to a plug-flow regime (strictly speak-

ing this is a pseudo-plug, that is a region which is at the yield stress so that it has solid-like behaviour but still deforms). Typically the plug-flow regime starts in the shallow deposition region below the couloir. When the slope is gentle so that the flow is slower and experiences less agitation from the base, and the flow depth and thus the overburden pressure are large, the full avalanche can transform into the warm plug regime (Fig. 8). Such a transition can occur also locally (Fig. 3I) or partially (Fig. 7C). This process may be explained by the granular nature of the flow and specifically by the balance between forces which promote aggregation and forces which induce fragmentation [*Steinkogler et al.*, 2015a; *Issler*, 2003]. In particular, the yield strength increases with particle cohesion and overburden pressure, whereas fragmentation forces such as shear and impact stresses increase with velocity and slope angle. To which extent a visco-plastic flow (a pure plug over a sheared layer, [*Kern et al.*, 2004]), a cohesive granular flow or a poly-disperse flow (thick sheared layer above a highly sheared layer, [*Rognon et al.*, 2008, 2007]) are more appropriate to represent such a transition is an actual debate [*Ancey*, 2007]. Additionally, one may consider segregation of faster and slower material, or colder and warmer material, inside the avalanche and mixing with warmer snow cover due to entrainment as a possible cause for the transition between WSR and WPR.

Finally, another important flow transition occurs when a cold avalanche transforms into a warm avalanche. Even though most of the snow flowing inside a PSA is cold, entrainment of deeper and warmer layers can raise the temperature to that of warm snow, with the result that the passage between warm and cold flow happens towards the avalanche tail and manifests itself with the formation of a creeping tail (Fig. 10). If, however, the full snow cover is warm, the flow regime transition can occur directly at the front and control

the complete flow dynamics. Indeed, the avalanche in Fig. 8 shows the typical features of a large PSA which transforms completely into a plug-flow below 1000 m range. It is remarkable, that this transition occurs in only a few seconds and within a distance of around 100 m, and is most likely the result of rain precipitation warming and wetting the snow cover at lower altitudes. Nearly all the potential energy in an avalanche will heat up the flowing snow due to friction. *Steinkogler et al.* [2015b] found a temperature increase of 0.3 °C per 100 m drop height, but entrainment of snow at lower altitudes and from deeper layers in the snow cover can be a much more effective mechanism to change the snow temperature inside the avalanche [*Steinkogler et al.*, 2014], since entrainment can increase the total flowing mass by an order of magnitude [*Sovilla et al.*, 2006].

7. Conclusions

The GEODAR system has collected data on 77 avalanche events since 2009/10. The avalanches show a wide variety of different dynamic behaviour and flow regimes. We have analysed the MTI flowing signatures such as lines and streaks or darker and light coloured spots, and conclude that streaks are the signature of internally moving features, and characteristic spots originate from the interaction of the avalanche with the terrain causing features such as standing waves. Further, the MTI plots show that there are three dominant stopping mechanisms, primarily determined by the snow temperature and liquid water content. These snow cover parameters mainly control the cohesion and cause the flowing snow to aggregate into granules or even clump together into large flow units. Cold snow tends to stop from the tail with a decrease in length of the flowing region behind the head, whereas warm snow tends to stop first at the front followed by a progressive pile up, and a large plug-flow unit can stop instantaneously.

Seven flow regimes have been defined on the basis of the GEODAR data. This list of flow regimes provides an exhaustive classification of the avalanches observed at Vallée de la Sionne. The GEODAR data can show the evolution of these flow regimes in time and space, and characterise transitions between them. While small to medium sized avalanches tend to be *simple* with only one flow regime, larger avalanches are *complex* and exhibit multiple flow regimes simultaneously. One reason for this is that large avalanches tend to cover a great range of altitudes ($> 1000\,\mathrm{m}$) and therefore experience a greater range of snow conditions.

Two of the seven flow regimes, the sliding slab and the snowball regime, are only of marginal interest in the big picture of an avalanche. But, the sliding and break up of slabs become important in respect to the entrainment process due to secondary releases [*Köhler et al.*, 2016]. And the rolling of snowballs can be seen as the "contact-less" granular limit of the warm shear regime. Rolling granules can not only reach farther runouts, but may even trigger secondary avalanches.

The other five flow regimes should be included in physically-based numerical models. For many purposes, for example hazard-zoning where good statistics are available, a physically based avalanche model is not always necessary. However, for scientific purposes where we wish to have models that correctly describe the underlying physics without containing empirically chosen fitting parameters, each of these regimes and transitions between them must be correctly modelled. Some of these regimes may be described by a single rheological model. For example, it may be possible to describe all the dense regimes CDR, WSR and WPR by a model including plasticity [*Ancey*, 2007] parameterised by temperature and granule size.

The intermittent regime (IR) is an important part of our classification system that may be helpful in explaining the longevity and mobility of powder snow avalanches [*Köhler et al.*, 2016], by significantly increasing the mass flux into the powder cloud and increasing the turbulent kinetic energy. New modelling concepts must be developed, since velocity and density variations [*Sovilla et al.*, 2015] may not be described with standard depth-averaged numerical approaches, though there can be good agreement [*Louge*, 2014]. Future work can build up on the descriptive terminology developed here, and connect rheological properties of snow to the expression of flow regimes by combine our results with the wide field of cohesive and non-cohesive granular flows.

Our observations of flow regimes in snow avalanches with the use of radar technology may also be important for other gravitational mass movements. For example, pyroclastic density currents may develop a similar flow regime as the intermittent regime of powder snow avalanches, but obtaining direct measurements in the hot ash is significantly harder. The advantage of using snow avalanches as an example flow process is the frequent return period and the possibility to control the release artificially.

To aid in the development of numerical models all of the data in this paper is released under a creative commons license. For users of this data, this paper also functions as a useful aid to understand the MTI plots and their features.

We also hope that this data set will attract the interest of those in the image-processing and machine-learning communities. If automatic algorithms for processing the GEODAR data can be developed, the radar data can be unambiguously and objectively interpreted without additional local point measurements. We hope that this work will spur the deployment of similar radar systems to study other mass flows and both improve scientific

understanding and have practical benefits for warning systems and road and infrastructure security.

Appendix A: List of acronyms

VdlS	Vallée de la Sionne
PRA	Release area around summit "Pra Roua"
CB	Release area ridge "Crêta Besse" with numbers 1 and 1/2, and summit with 2
GEODAR	GEOphysical flow dynamics using pulsed Doppler radAR
FMCW	Frequency Modulated Continuous Wave
MTI	Moving target identification, *e.g.* used in GEODAR images
VDS2	Weather station "Donin du jour" at 2390 m a.s.l., subscript $_t$
VDS3	Weather station close to the pylon at 1680 m a.s.l., subscript $_b$
WPR	Warm plug regime
CDR	Cold dense regime
WSR	Warm shear regime
IR	Intermittent regime
SBR	Snowball regime
SSR	Sliding slab regime
SR	Suspension regime
PSA	Powder snow avalanche

Appendix B: GEODAR data repository

All the GEODAR data discussed in this paper and listed in Table 1 are open access and stored in the Zenodo (`https://zenodo.org/`) data repository, which is financed by the Horizon 2020 project OpenAIRE and hosted by CERN. The associated entry can be accessed via:

McElwaine*, J. N., A. Köhler*, B. Sovilla, M. Ash, and P. V. Brennan (2017), GEODAR data of snow avalanches at Vallée de la Sionne: Seasons 2010/11, 2011/12, 2012/13 & 2014/15 [Data set]. *Zenodo.* doi:10.5281/zenodo.1042108 . *equally contributing authors

The archive contains processed GEODAR data namely the MTI plots, plus some derived data such as the 1D thalweg, the projected trajectory $s(t)$ and the down-slope velocity $\dot{s}(t)$ of the front or surge. A document serves as metadata and contains details related to GEODAR. We give a comprehensive description of the different GEODAR versions, more technical details to the applied processing steps, the MTI filtering, the HDF5 data format and how to access the data in the container. Finally, the bibliography list of all GEODAR related publications serves as references.

Even though the data is generally open access, we highly recommend to contact the authors prior to usage. Even though we gained a substantial knowledge about the signal interpretation, the data is still not straightforward to use. We believe that only a culture of open discussion and collaboration can make the most out of this invaluable data set.

Supplementary data as the meteo data and snowpack simulations used in this paper are not part of the data repository, but are made available upon request.

Notes

1. We are using *unit* in its geological sense. *Units* are the basic units of geologic mapping and refer to regions with similar properties.

References

Ammann, W. J., A new swiss test-site for avalanche experiments in the Vallée de la Sionne/Valais, *Cold Reg. Sci. Tech.*, *30*(1), 3–11, doi:10.1016/S0165-232X(99)00010-5, 1999.

Ancey, C., Plasticity and geophysical flows: A review, *J. Non-Newtonian Fluid Mech.*, *142*(1–3), 4–35, doi:10.1016/j.jnnfm.2006.05.005, 2007.

Ash, M., P. V. Brennan, K. Chetty, J. N. McElwaine, and C. J. Keylock, FMCW Radar Imaging of Avalanche-like Snow Movements, in *Proceedings of the 2010 IEEE Radar Conf.*, pp. 102–107, IEEE, Arlington, Va., doi:10.1109/RADAR.2010.5494643, 2010.

Ash, M., M. A. Tanha, P. V. Brennan, A. Köhler, J. N. McElwaine, and C. J. Keylock, Practical implementation of a 16-channel C-band phased array radar receiver, in *Proceedings of the 2015 IEEE Radar Conf.*, pp. 66–70, IEEE, Sandton, South Africa, doi:10.1109/RadarConf.2015.7411856, 2015.

Bartelt, P., and B. W. McArdell, Instruments and Methods Granulometric investigations of snow avalanches, *J. Glaciol.*, *55*(193), 829–833, doi:10.3189/002214309790152384, 2009.

Brennan, P. V., M. Ash, F. M. Isa, C. J. Keylock, and J. N. McElwaine, Advanced Radar Imaging of Geophysical Flows, in *IASME/WSEAS Int. Conf. on Geology and Seismology*, pp. 144–147, 2009.

De Quervain, M. R., L. De Crecy, E. R. LaChapelle, K. Losev, and M. Shoda, Avalanche classification, *Hydrol. Sci. Bull.*, *18*(4), 391–402, doi:10.1080/02626667309494054, 1973.

Faug, T., P. Childs, E. Wyburn, and I. Einav, Standing jumps in shallow granular flows down smooth inclines, *Phys. Fluids*, *27*(7), 073304, doi:10.1063/1.4927447, 2015.

Gauer, P., D. Issler, K. Lied, K. Kristensen, and F. Sandersen, On snow avalanche flow regimes: Inferences from observations and measurements, *International Snow Science Workshop, Whistler, Canada*, pp. 717–723, 2008.

Gray, J. M. N. T., Y.-C. Tai, and S. Noelle, Shock waves, dead zones and particle-free regions in rapid granular free-surface flows, *J. Fluid Mech.*, *491*, 161–181, doi: 10.1017/S0022112003005317, 2003.

Gubler, H., and M. Hiller, The use of microwave FMCW radar in snow and avalanche research, *Cold Reg. Sci. Tech.*, *9*(2), 109–119, doi:10.1016/0165-232X(84)90003-X, 1984.

Hákonardóttir, K. M., A. J. Hogg, J. Batey, and A. W. Woods, Flying avalanches, *Geophys. Res. Lett.*, *30*(23), 2191, doi:10.1029/2003GL018172, 2003.

Hopfinger, E. J., Snow avalanches motion and related phenomena, *Annu. Rev. Fluid Mech.*, *15*, 47–96, doi:10.1146/annurev.fl.15.010183.000403, 1983.

Issler, D., Modelling of snow entrainment and deposition in powder-snow avalanches, *Ann. Glaciol.*, *26*(1), 253–258, doi:10.1017/S0260305500014919, 1998.

Issler, D., Experimental Information on the Dynamics of Dry-Snow Avalanches, in *Dynamic Response of Granular and Porous Materials under Large and Catastrophic Deformations*, edited by K. Hutter and N. Kirchner, pp. 109–160, Springer, doi: 10.1007/978-3-540-36565-5_4, 2003.

Kern, M. A., F. Tiefenbacher, and J. N. McElwaine, The rheology of snow in large chute flows, *Cold Reg. Sci. Tech.*, *39*(2–3), 181–192, doi:10.1016/j.coldregions.2004.03.006, 2004.

Keylock, C. J., M. Ash, N. Vriend, P. V. Brennan, J. N. McEwaine, and B. Sovilla, Looking inside an avalanche using a novel radar system, *Geology Today*, *30*(1), 21–25,

doi:10.1111/gto.12033, 2014.

Köhler, A., J. N. McElwaine, B. Sovilla, M. Ash, and P. V. Brennan, The dynamics of surges in the 3 February 2015 avalanches in Vallée de la Sionne, *J. Geophys. Res.*, *121*(11), 2192–2210, doi:10.1002/2016JF003887, 2016.

Lehning, M., P. Bartelt, B. Brown, and C. Fierz, A physical SNOWPACK model for the Swiss avalanche warning part III: meteorological forcing, thin layer formation and evaluation, *Cold Reg. Sci. Tech.*, *35*(3), 169–184, doi:10.1016/S0165-232X(02)00072-1, 2002.

Louge, M., The surprising relevance of a continuum description to granular clusters, *J. Fluid Mech.*, *742*, 1–4, doi:10.1017/jfm.2013.650, 2014.

Naaim, M., Y. Durand, N. Eckert, and G. Chambon, Dense avalanche friction coefficients: influence of physical properties of snow, *J. Glaciol.*, *59*(216), 771–782, doi:10.3189/ 2013JoG12J205, 2013.

Pérez-Guillén, C., B. Sovilla, E. Suriñach, M. Tapia, and A. Köhler, Deducing avalanche size and flow regimes from seismic measurements, *Cold Reg. Sci. Tech.*, *121*, 25–41, doi:10.1016/j.coldregions.2015.10.004, 2015.

Rognon, P. G., J.-N. Roux, M. Naaim, and F. Chevoir, Dense flows of bidisperse assemblies of disks down an inclined plane, *Phys. Fluids*, *19*(5), 058101, doi:10.1063/1.2722242, 2007.

Rognon, P. G., J.-N. Roux, M. Naaim, and F. Chevoir, Dense flows of cohesive granular materials, *J. Fluid Mech.*, *596*, 21–47, doi:10.1017/S0022112007009329, 2008.

Salm, B., and H. Gubler, Measurement and Analysis of the Motion of Dense Flow Avalanches, *Ann. Glaciol.*, *6*, 26–34, doi:10.1017/S0260305500009939, 1985.

Schaerer, P., and A. Salway, Seismic and impact-pressure monitoring of flowing avalanches, *J. Glaciol.*, *26*(94), 179–187, doi:10.1017/S0022143000010716, 1980.

Schmid, L., A. Heilig, C. Mitterer, J. Schweizer, H. Maurer, R. Okorn, and O. Eisen, Continuous snowpack monitoring using upward-looking ground-penetrating radar technology, *J. Glaciol.*, *60*(221), 509–525, doi:10.3189/2014JoG13J084, 2014.

Sovilla, B., P. Burlando, and P. Bartelt, Field experiments and numerical modeling of mass entrainment in snow avalanches, *J. Geophys. Res.*, *111*, F03007, doi:10.1029/2005JF000391, 2006.

Sovilla, B., J. N. McElwaine, M. Schaer, and J. Vallet, Variation of deposition depth with slope angle in snow avalanches: Measurements from Vallée de la Sionne, *J. Geophys. Res.*, *115*, F02016, doi:10.1029/2009JF001390, 2010.

Sovilla, B., J. N. McElwaine, and M. Y. Louge, The structure of powder snow avalanches, *C. R. Phys.*, *16*(1), 97–104, doi:10.1016/j.crhy.2014.11.005, 2015.

Sovilla, B., et al., The full-scale avalanche dynamics test site Vallée de la Sionne, *International Snow Science Workshop, Grenoble–Chamonix, France*, pp. 1350–1357, 2013.

Steinkogler, W., B. Sovilla, and M. Lehning, Influence of snow cover properties on avalanche dynamics, *Cold Reg. Sci. Tech.*, *97*, 121–131, doi:10.1016/j.coldregions.2013.10.002, 2014.

Steinkogler, W., J. Gaume, H. Löwe, B. Sovilla, and M. Lehning, Granulation of snow: From tumbler experiments to discrete element simulations, *J. Geophys. Res.*, *120*(6), 1107–1126, doi:10.1002/2014JF003294, 2015a.

Steinkogler, W., B. Sovilla, and M. Lehning, Thermal energy in dry snow avalanches, *Cryosphere*, *9*(5), 1819–1830, doi:10.5194/tc-9-1819-2015, 2015b.

Swiss Geoportal, Available at `https://map.geo.admin.ch/?topic=ech&X=127547.50&Y=594372.50&zoom=8`, accessed: 30 September 2015, 2015.

Tanha, M. A., P. V. Brennan, M. Ash, A. Köhler, and J. N. McElwaine, Overlapped Phased Array Antenna for Avalanche Radar, *IEEE Trans. Antennas.*, *65*(8), 4017–4026, doi:10.1109/TAP.2017.2712183, 2017.

Turnbull, B., and P. Bartelt, Mass and Momentum Balance Model of a Mixed Flowing/Powder Snow Avalanche, *Surv. Geophys.*, *24*(5–6), 465–477, doi:10.1023/B:GEOP. 0000006077.82404.84, 2003.

Turnbull, B., and J. N. McElwaine, A comparison of powder snow avalanches at Vallée de la Sionne with plume theories, *J. Glaciol.*, *53*(180), 30–40, doi:10.3189/ 172756507781833938, 2007.

UNESCO, Avalanche atlas: Illustrated international avalanche classification, *Tech. rep.*, International Commission on Snow and Ice, UNESCO, Paris, 1981.

Voellmy, A., Über die Zerstörungskraft von Lawinen (On the destructive forces of avalanches), *Schweizerische Bauzeitung*, *73*(15), 212–217, 1955.

Vriend, N. M., J. N. McElwaine, B. Sovilla, C. J. Keylock, M. Ash, and P. V. Brennan, High-resolution radar measurements of snow avalanches, *Geophys. Res. Lett.*, *40*(4), 727–731, doi:10.1002/grl.50134, 2013.

Wever, N., C. Fierz, C. Mitterer, H. Hirashima, and M. Lehning, Solving Richards Equation for snow improves snowpack meltwater runoff estimations in detailed multi-layer snowpack model, *Cryosphere*, *8*(1), 257–274, doi:10.5194/tc-8-257-2014, 2014.

Table 1. List of avalanche events recorded with GEODAR system. For a detailed description see subsection 2.6. The first block summarises metadata including release area, runout, stopping signature and velocity v_s. The second block contains the availability of additional data from cameras, Caverns A and B, and the pylon (C). The third block gives meteorological and nivological conditions.

| SLF-Nr	GEODAR timestamp	Release	Altitude [m]	Runout [m]	Stop	Slope [°]	v_s [m s^{-1}]	Img	A	B	C	TS$_b$ [°C]	TS$_t$ [°C]	LWC$_b$ [%]	LWC$_t$ [%]	HN$_b$ [cm]	HN$_t$ [cm]
20113002	2010-12-06-07-46-21	CB2	>2600	360	A	21	15	1	0	0	0	-	-4.3	-	0.0	-	27
20113003	2010-12-06-18-36-18	PRA	>2500	490	A	23	16	1	0	1	1	-	-2.3	-	0.0	-	41
20113004	2010-12-07-03-36-43	CB1/2	>2600	150	-	23	8	1	1	1	1	-	-1.9	-	0.0	-	54
*20123013	2011-12-19-15-16-02	CB1/2	~2550	1560	A	30	13	0	-	-	-	-	-11.3	-	0.0	-	125
20123023	2011-12-30-23-55-22	CB1/2	>2100	670	A	23	15	0	0	1	-	-	-9.1	-	0.0	-	50
20123024	2011-12-31-06-59-34	unknown	-	1820	A	-	15	0	-	-	-	-	-7.0	-	0.0	-	56
20123026	2011-12-31-07-44-25	CB1	>2300	850	A	22	14	0	0	1	-	-	-6.5	-	0.0	-	58
20123028	2011-12-31-09-01-41	unknown	-	670	A	-	19	0	0	1	-	-	-6.1	-	0.0	-	61
20123029	2012-01-02-21-22-15	PRA	1906	995	C	26	2	2	-	-	-	-	-4.5	-	0.0	-	13
20123031	2012-01-04-07-21-42	CB1	>2100	965	C	25	14	0	0	1	0	-	-4.3	-	0.0	-	16
20123032	2012-01-04-07-42-50	CB1/2	>2600	955	C	25	19	0	1	1	0	-	-4.2	-	0.0	-	16
20123035	2012-01-05-16-45-21	CB1/2	>2650	150	A	18	28	1	1	1	1	-	-5.1	-	0.0	-	26
20123040	2012-01-10-00-03-06	PRA	2264	675	B	23	16	2	-	-	-	-	-7.8	-	0.0	-	0
20123041	2012-01-12-17-19-07	CB1/2	2500	1255	B	30	18	2	-	-	-	-	-6.1	-	0.0	-	0
20123042	2012-01-13-02-42-41	CB1/2	2014	1000	C	26	2	2	-	-	-	-	-7.4	-	0.0	-	0
20123048	2012-02-03-16-25-32	CB1	2051	850	B	22	16	2	-	-	-	-	-8.8	-	0.0	-	0
20123051	2012-02-24-12-24-47	CB1/2	2586	1395	-	38	6	2	-	-	-	-	-7.5	-	0.0	-	0
20123053	2012-02-29-16-48-02	CB1	2394	940	C/B	24	15	2	-	-	-	-	-4.0	-	0.6	-	0
20123055	2012-03-01-14-44-36	PRA	2540	930	C	24	9	2	0	0	-	-	-3.0	-	0.8	-	0
20123060	2012-03-15-10-56-28	PRA	2458	950	B	25	17	2	0	0	-	-	-1.9	-	0.1	-	0
20133003	2012-12-04-04-46-05	CB1	>2450	545	A	23	25	1	0	1	1	-0.8	-4.4	0.0	0.0	50	59
20133005	2012-12-06-01-54-50	CB1	>2200	890	A	23	16	0	0	0	0	-5.5	-9.8	0.0	0.0	87	94
20133006	2012-12-07-14-00-39	unknown	-	1625	A	-	12	0	-	-	-	-5.5	-10.1	0.0	0.0	79	102
20133007	2012-12-10-08-12-49	CB1/2	>2050	825	A	22	14	0	0	1	-	-4.4	-9.1	0.0	0.0	34	35
20133018	2013-02-01-16-52-45	CB1/2	>2500	880	C	22	10	1	1	1	-	0.0	-2.2	1.7	0.0	15	35
20133019	2013-02-01-17-14-50	CB1/2	>2450	200	C	19	1	1	1	1	1	0.0	-2.2	1.7	0.0	15	35
20133020	2013-02-01-20-18-46	CB2	>2600	155	C	18	2	1	-	1	-	0.0	-2.2	1.8	0.0	15	44
20133021	2013-02-02-05-27-31	PRA	>2450	180	C	18	6	1	0	1	1	-0.0	-2.6	1.9	0.0	15	69
20133022	2013-02-02-15-38-13	CB1	2069	960	B	25	10	1	-	1	-	-0.3	-5.8	1.6	0.0	25	79
20133023	2013-02-05-21-13-35	CB1	~2250	1190	A	30	16	0	0	1	-	-1.4	-6.3	0.2	0.0	44	92
20133024	2013-02-05-23-31-53	CB1/2	~2600	460	A	22	18	0	1	1	0	-2.5	-8.1	0.0	0.0	52	99
20133025	2013-02-19-13-13-31	CB1/2	2506	1775	A	29	8	2	-	-	-	-2.4	-6.5	0.0	0.0	0	0
20133028	2013-03-02-11-46-45	CB1/2	2029	940	B	24	12	2	-	-	-	-0.8	-5.8	0.1	0.0	0	0
20133030	2013-03-03-11-29-11	CB1/2	2608	1940	-	34	10	2	-	-	-	-0.6	-6.1	0.4	0.0	0	0
20133031	2013-03-03-12-23-33	CB1/2	2602	1900	-	31	10	2	-	-	-	-0.6	-5.4	0.4	0.0	0	0
20133037	2013-03-18-23-50-57	CB1/2	>2550	1720	A	28	18	0	1	-	-	-1.1	-6.0	0.0	0.0	16	45
20133038	2013-03-19-03-24-48	unknown	-	1125	A	-	16	0	-	-	-	-1.7	-7.3	0.0	0.0	24	57
20133040	2013-03-19-04-21-42	CB1	>2100	1050	A	27	19	0	0	0	0	-1.7	-7.8	0.0	0.0	24	58
20133041	2013-03-22-10-03-29	CB1/2	2547	1525	A	30	7	1	1	0	-	-0.0	-3.1	0.6	0.0	38	40
20133043	2013-04-06-18-35-09	CB1/2	2486	1725	C	28	2	2	-	-	-	0.0	-1.7	2.6	0.0	0	0
20133044	2013-04-06-19-23-47	CB1/2	2488	1010	B	26	20	2	-	-	-	0.0	-1.7	2.6	0.0	0	0
20133046	2013-04-10-15-07-55	PRA	2350	990	C	26	6	2	-	-	-	0.0	-1.0	2.8	0.1	29	44
20133047	2013-04-12-13-33-47	PRA	2319	785	C	21	17	2	-	-	-	0.0	-0.5	3.1	0.1	0	37
20133048	2013-04-13-04-06-44	CB1	2432	775	C/B	21	1	2	-	-	-	-0.1	-1.8	1.8	0.0	10	51
20133049	2013-04-13-12-37-24	CB1	2300	965	C/B	25	5	2	-	0	-	0.0	-0.4	3.2	0.2	10	51
20133050	2013-04-13-14-19-46	CB1/2	2380	995	B/C	26	11	2	-	0	-	0.0	-0.4	3.2	0.3	10	51
20133051	2013-04-13-23-59-42	CB1	2215	975	C/B	25	4	2	-	0	-	-0.2	-0.9	1.8	0.1	10	51
20133052	2013-04-14-11-25-56	CB1/2	2501	1795	B/C	29	18	2	-	0	-	0.0	-0.6	3.5	0.2	0	14
20133053	2013-04-14-22-49-51	CB1/2	2415	960	C/B	25	4	2	-	0	-	-0.0	-0.3	2.1	1.3	0	0
20140011	2014-02-13-17-37-30	CB1/2	>2450	1150	A	29	13	0	-	-	-	-2.2	-3.8	0.0	0.0	27	28
20140012	2014-02-13-19-21-32	CB1/2	>2500	160	A	18	30	0	1	1	1	-2.2	-4.3	0.0	0.0	32	38
20140013	2014-02-20-11-15-05	CB1/2	2596	1890	A	32	9	2	-	-	-	-1.2	-3.2	0.0	0.0	18	20
20140014	2014-02-21-14-53-19	CB1	2210	770	C/B	21	1	2	-	-	-	-0.8	-1.8	0.0	0.0	0	0
20140016	2014-03-11-11-54-57	CB1	2042	1000	C	26	6	2	-	-	-	-0.5	-2.0	0.2	0.1	0	0
20140017	2014-03-12-13-09-43	PRA	~2250	1160	B/C	34	9	0	0	0	-	-0.4	-1.8	0.4	0.2	0	0
20140019	2014-03-13-14-30-06	CB1/2	2483	1610	C	30	6	2	-	-	-	-0.0	-1.1	1.1	0.7	0	0
20150003	2014-12-27-20-18-49	CB1	~2550	600	A	24	22	0	0	1	1	-6.4	-9.2	0.0	0.0	57	73
20150004	2014-12-27-22-38-15	unknown	-	1105	A	-	19	0	0	0	-	-6.7	-9.7	0.0	0.0	61	73
20150009	2015-01-29-05-18-08	CB2	~2550	710	A	18	18	0	0	1	-	-1.3	-5.3	0.0	0.0	21	26
20150011	2015-01-29-06-22-02	CB1/2	>2450	860	B	22	24	0	1	1	-	-1.3	-5.4	0.0	0.0	22	31
20150013	2015-01-30-02-12-22	CB2	~2650	100	A	18	29	0	0	1	1	-3.6	-7.3	0.0	0.0	42	78
20150015	2015-01-30-20-58-55	CB1/2	>2450	1085	A	28	12	0	1	1	-	-5.2	-10.5	0.0	0.0	51	93
*20150016	2015-02-03-10-20-16	PRA	2510	100	-	18	34	2	0	1	1	-4.2	-10.0	0.0	0.0	50	97
*20150017	2015-02-03-11-45-30	CB1	2574	110	-	18	43	2	0	1	1	-2.0	-8.7	0.0	0.0	50	97
*20150019	2015-02-03-11-54-44	CB1/2	2606	870	A	22	8	2	1	1	-	-2.0	-8.7	0.0	0.0	50	97
*20150020	2015-02-03-12-04-39	CB2	2649	150	A	18	17	2	0	1	1	-2.0	-8.7	0.0	0.0	50	97
*20150022	2015-02-03-12-14-47	CB1/2	2607	970	A	25	16	2	-	-	-	-2.0	-8.7	0.0	0.0	50	97
20150028	2015-03-11-12-16-07	CB1/2	2471	1835	-	30	5	2	-	-	-	0.0	-1.4	0.0	0.1	-	0
20150035	2015-04-03-11-42-26	CB1	>2400	945	C/B	25	1	0	0	0	-	-	-0.1	-	0.1	-	78
20150037	2015-04-03-12-39-00	CB1/2	>2450	1220	B	30	3	0	0	0	-	-	-0.1	-	0.2	-	78
20150038	2015-04-03-13-04-39	unknown	-	1985	-	-	5	0	-	-	-	-	-0.1	-	0.2	-	78
20150040	2015-04-08-22-35-13	CB1/2	2497	765	C	21	1	2	-	-	-	-	-1.1	-	0.1	-	23
20150043	2015-04-09-17-21-45	CB1	2212	955	B	25	4	2	-	-	-	-	-0.2	-	1.4	-	23
20150044	2015-04-10-16-11-33	CB1/2	~2400	1170	C	29	10	0	0	0	-	-	-0.1	-	1.8	-	0
20150046	2015-04-11-10-05-55	CB1/2	2481	1890	-	31	5	2	-	-	-	-	0.0	-	1.7	-	0
20150047	2015-04-11-14-37-05	PRA	2215	1100	C	28	10	2	-	-	-	-	0.0	-	1.7	-	0
20150048	2015-04-12-00-08-39	CB1	2376	1315	B	34	8	2	-	-	-	-	-0.2	-	1.5	-	0
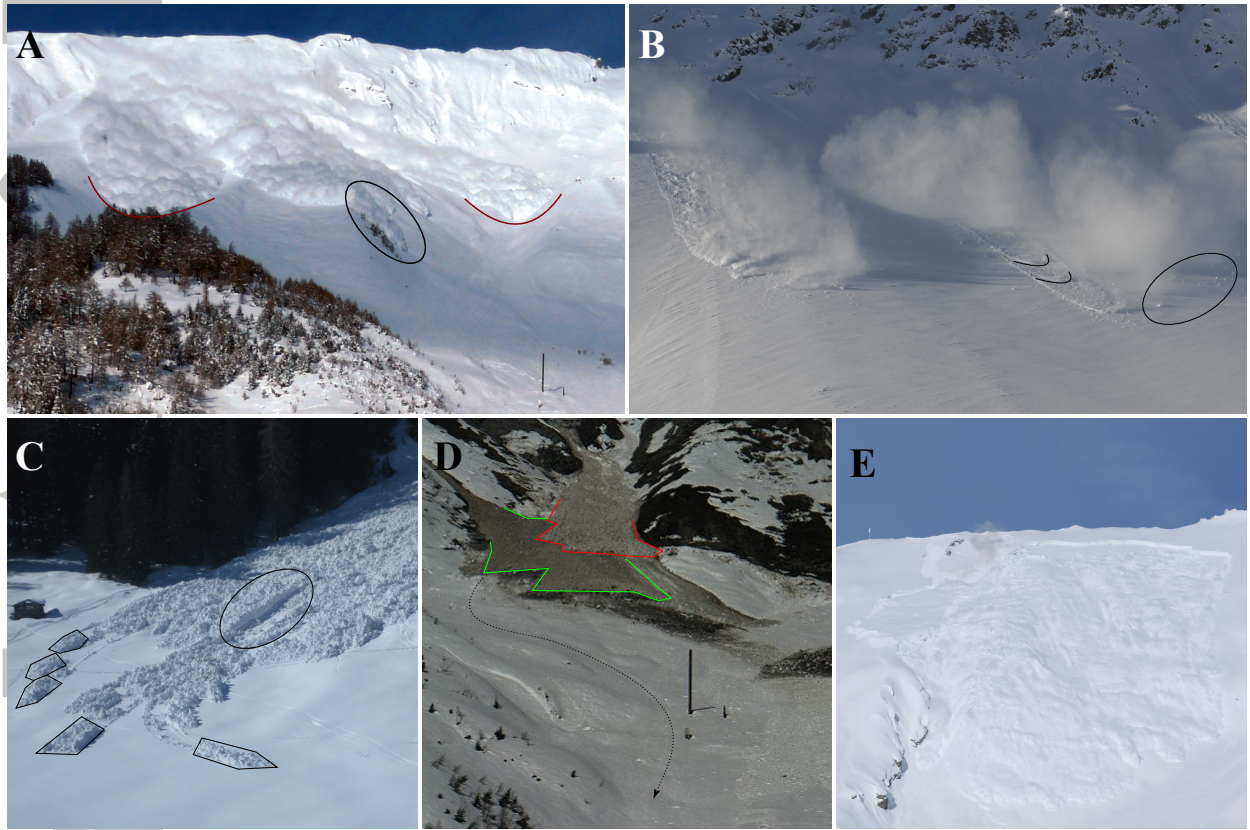
Figure 1. Variety of snow avalanches. Panel A: Large powder snow avalanche with separate fronts (VdlS, #15-0016, Fig. 3F). B: Cold dense avalanche with roll-waves, and fragments rolling independently (Flüelapass, 2011, *Steinkogler et al.* [2015b]). C: Warm plug avalanche with levées and large flow units (Davos, 2015). D: Two fronts of warm shear avalanche with single granules passing the pylon (VdlS, #12-3060, Fig. 7). E: Fracturing cold slab and the formation of a suspension cloud (VdlS, #15-0020).
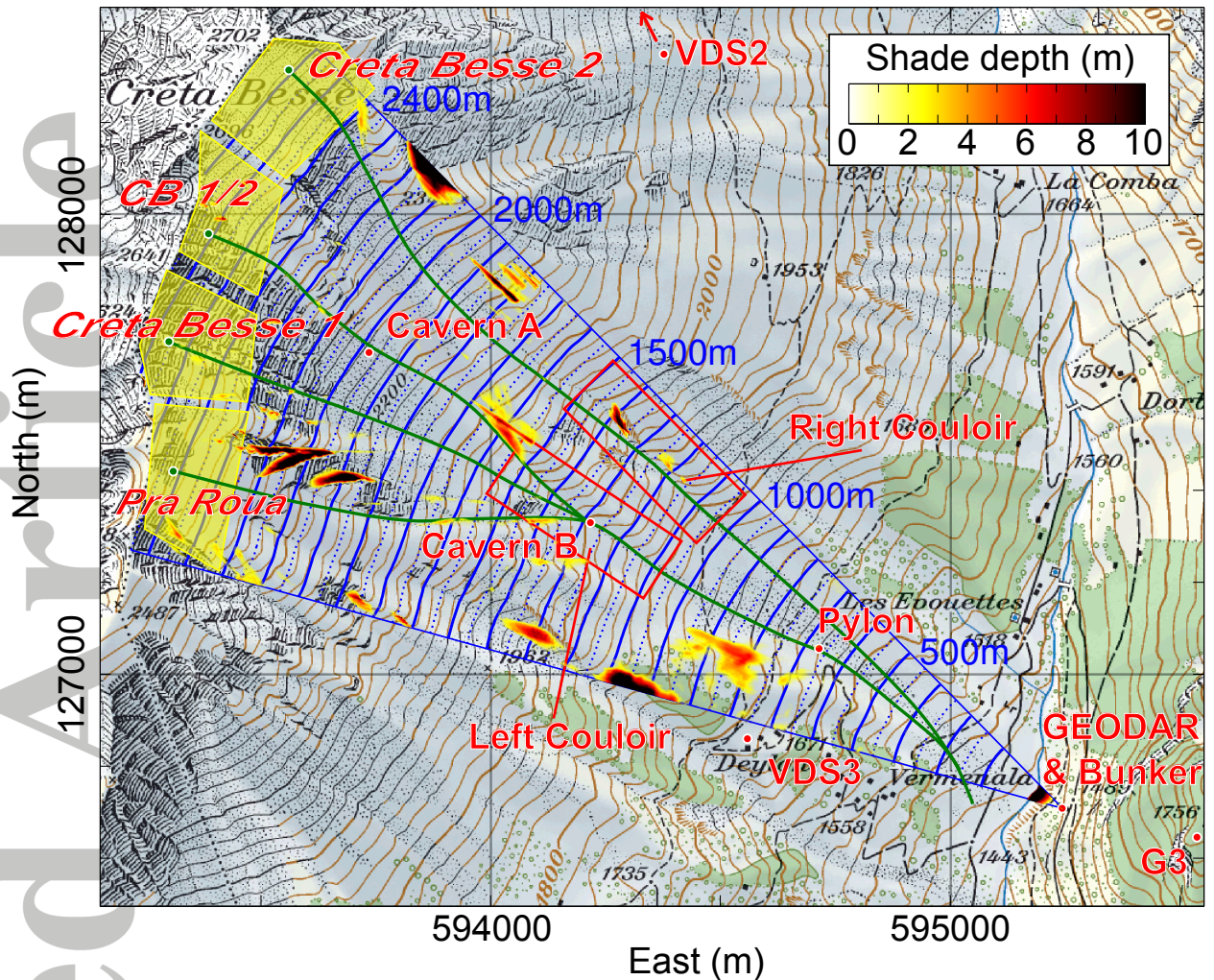
Figure 2. Overview of the Vallée de la Sionne (VdlS) test-site. Blue contour lines cover the area observed by GEODAR and indicate the radar range. Areas not visible to GEODAR are coloured with the yellow–black colour map giving the vertical shadow depth. Red points mark the locations of the pylon, the caverns, the meteo stations and the bunker hosting the GEODAR system. The four typical release areas are outlined in yellow, and green dots mark the representative coordinate for PRA, CB1, CB1/2 and CB2 release locations giving the typical thalweg as green line. The original map is obtained from the *Swiss Geoportal* [2015] in Swiss coordinate system CH1903 (SRID 21781). Figure reproduced from *Köhler et al.* [2016].
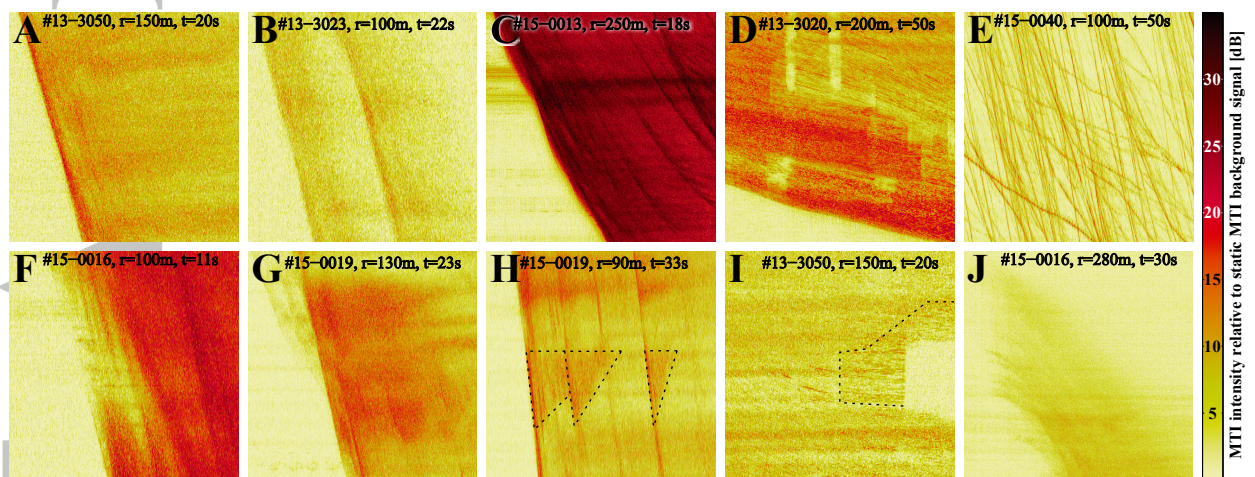
Figure 3. Common GEODAR flowing signatures of snow avalanches. A–E show streak signatures indicating structures flowing with the avalanche. F–J show signatures of flow structures which are connected to a location in the avalanche path. Avalanche number and scale in range r (y-axis) and time t (x-axis) are include in each panel. The colour scale of logarithmic MTI intensity is the same in all panels.
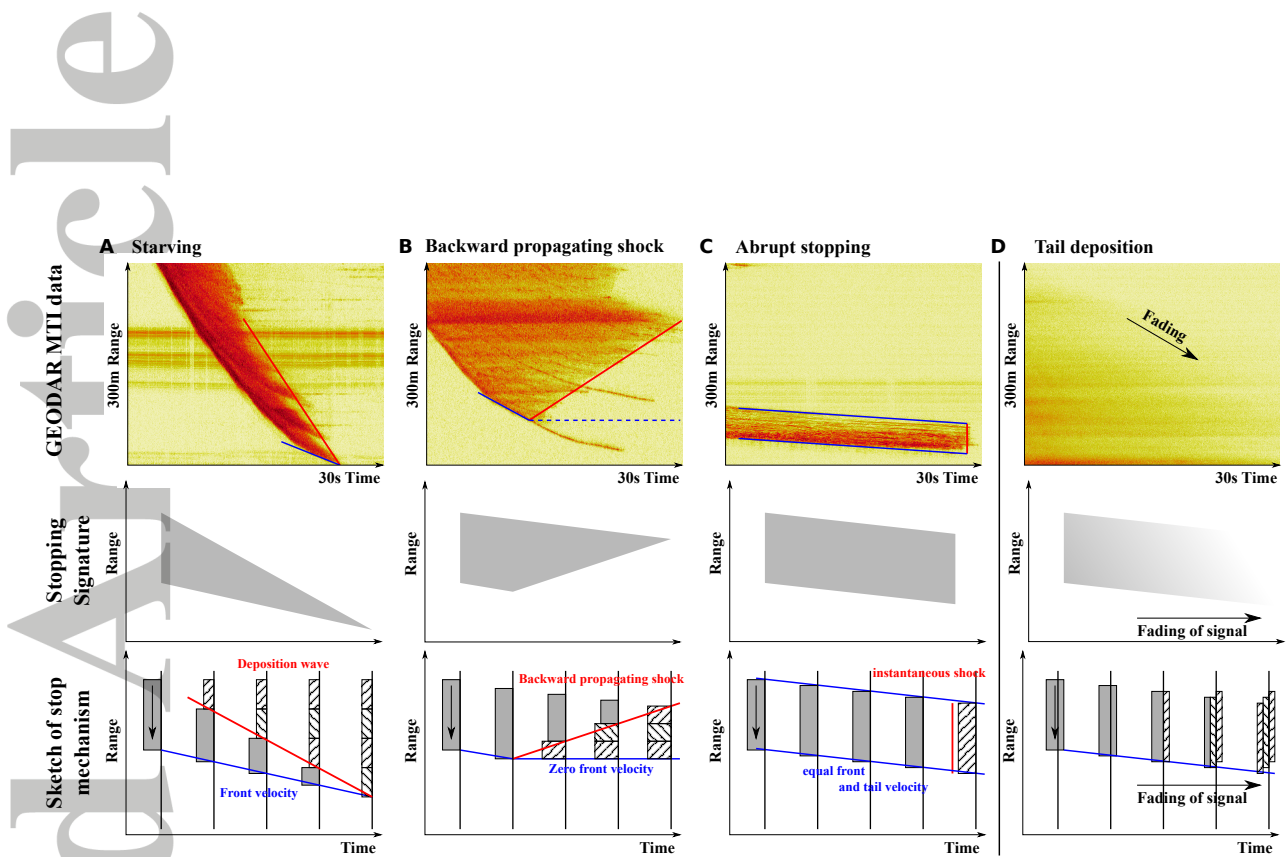
Figure 4. Top row: Four stopping signatures of avalanches measured in VdlS: (A) starving (#11-3002), (B) backward propagating shock (#12-3048), (C) abrupt stopping (#14-0014), and (D) tail deposition (#15-0009). Middle row: The characteristic stopping signature is shown below as a synthetic MTI. Bottom row: Sketch of the corresponding stopping mechanism. Only moving parts (grey), but not deposits (striped), will show up in the synthetic MTI. The MTI is in fact the grey area of the sketch.
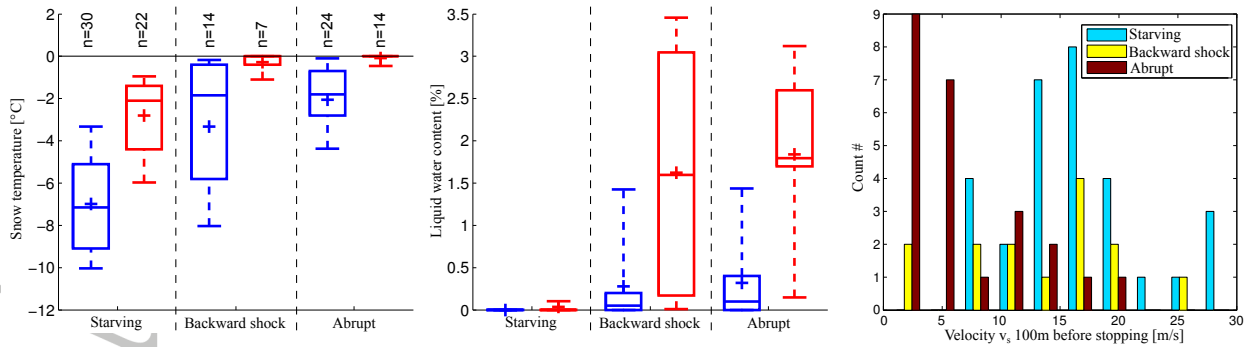
Figure 5. Correlation of stopping mechanisms with snow cover properties and front velocity. Box plots for snow temperature (left) and liquid water content (middle) correspond to quantities averaged over the upper-most $0.5\,\mathrm{m}$ of the snowpack. The snow conditions in the release area are represented by the weather station VDS2 (blue), and for the deposit region by the weather station VDS3 (red). The number of data per box are given by n, cross gives the mean, line is the median, the box spans the inter-quartile range and the whiskers show the 9 to 91 percentiles. Right: Histogram of v_s, the velocity $100\,\mathrm{m}$ before the avalanches stop.
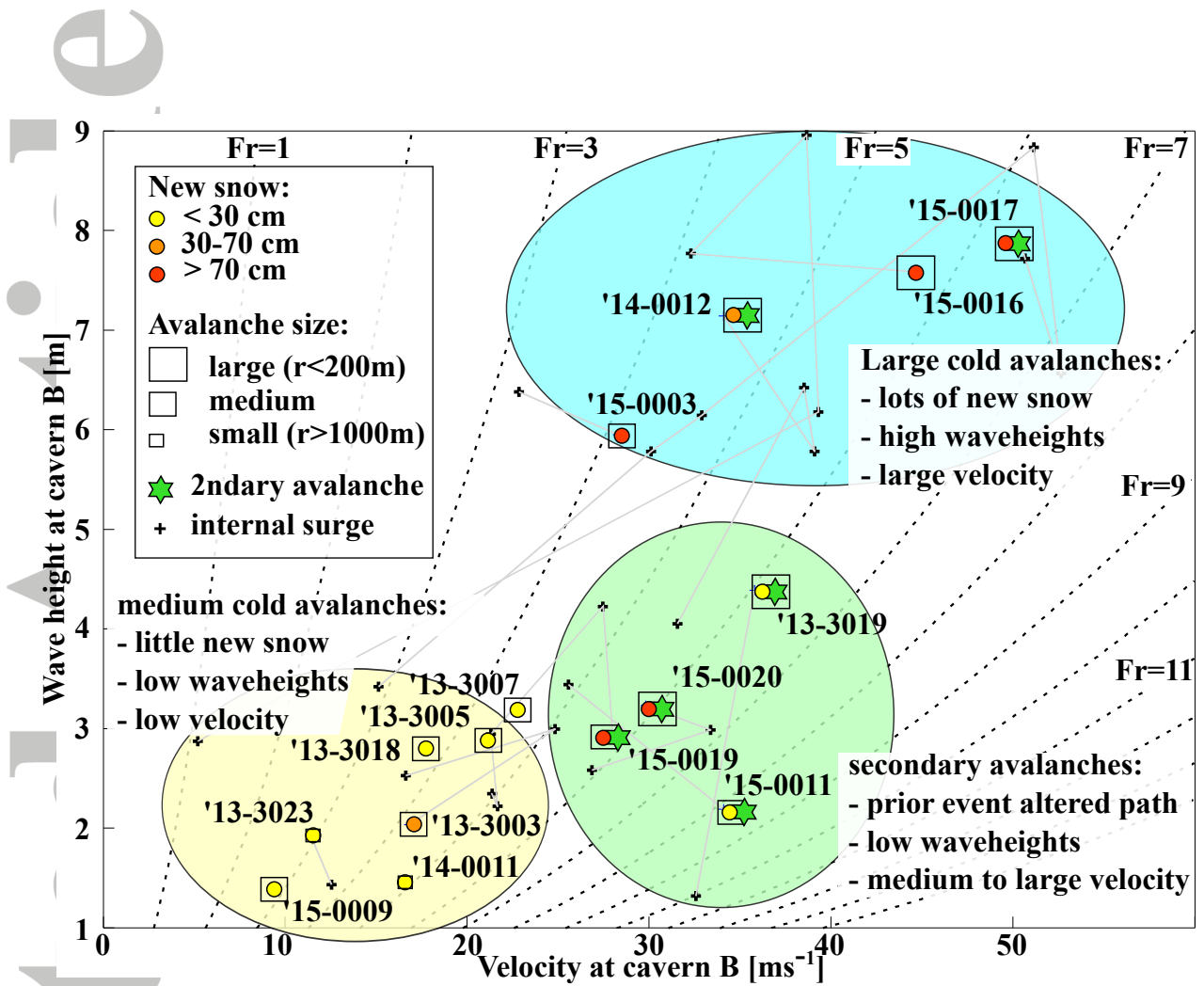
Figure 6. Flow heights of cold avalanches as a function of the velocity at Cavern B. The front is indicated by symbols, which give the amount of new snow (round), the avalanche size in runout range (squares) and whether it was a secondary avalanche (star). Small black crosses belong to internal surges, and grey lines connect the consecutive surges with the front. Froude numbers Fr are shown with black dashed lines in the background.
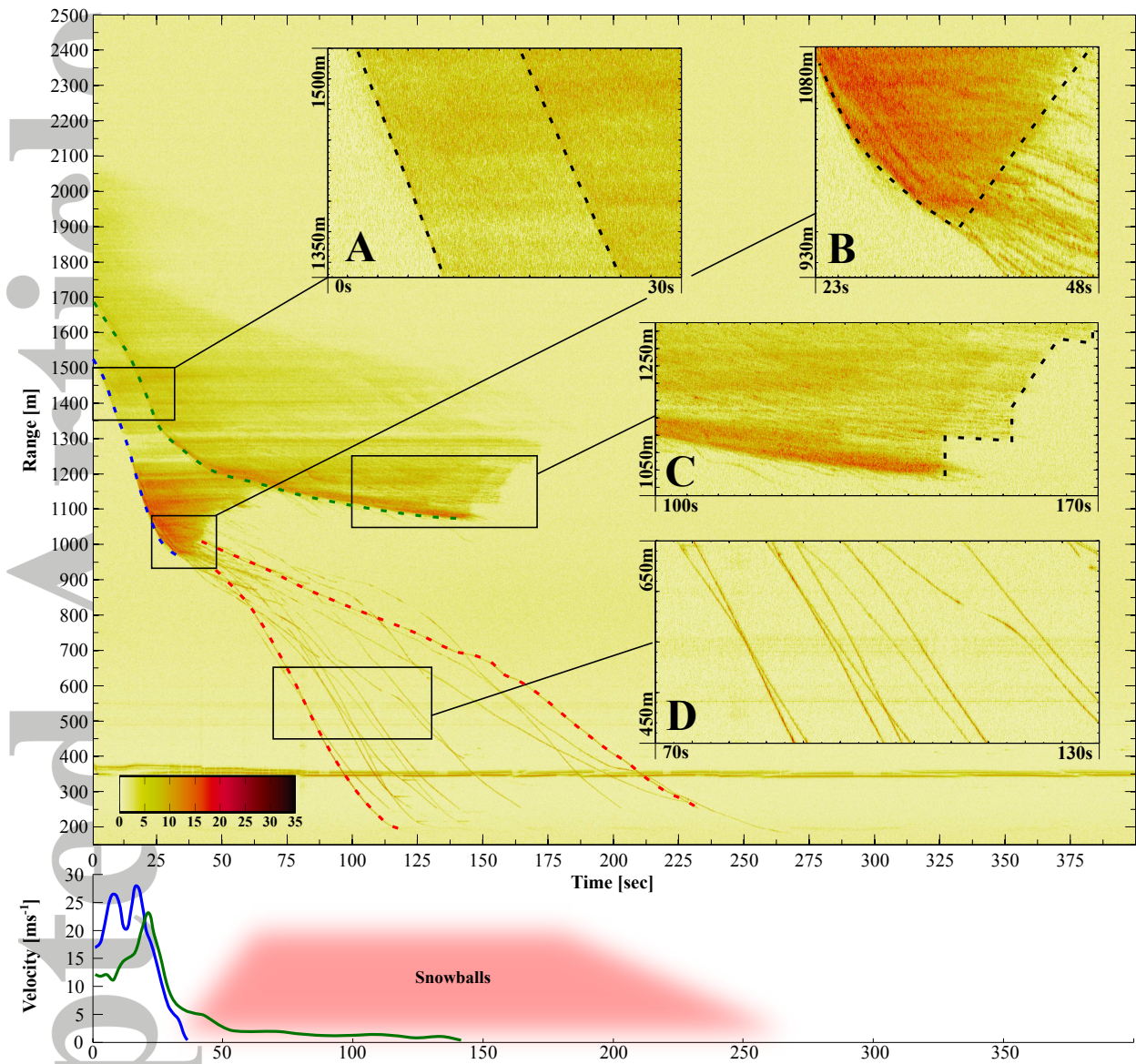
Figure 7. Avalanche #12-3060 naturally released on 15 March 2012 from Pra Roua. This avalanche is mostly representative of the warm shear regime (WSR). The avalanche release was not recorded and GEODAR first captured the avalanche when two laterally displaced fronts entered the couloir. While most of the avalanche stopped at the end of the couloir, snowballs continued to roll for up to one kilometre (SBR).
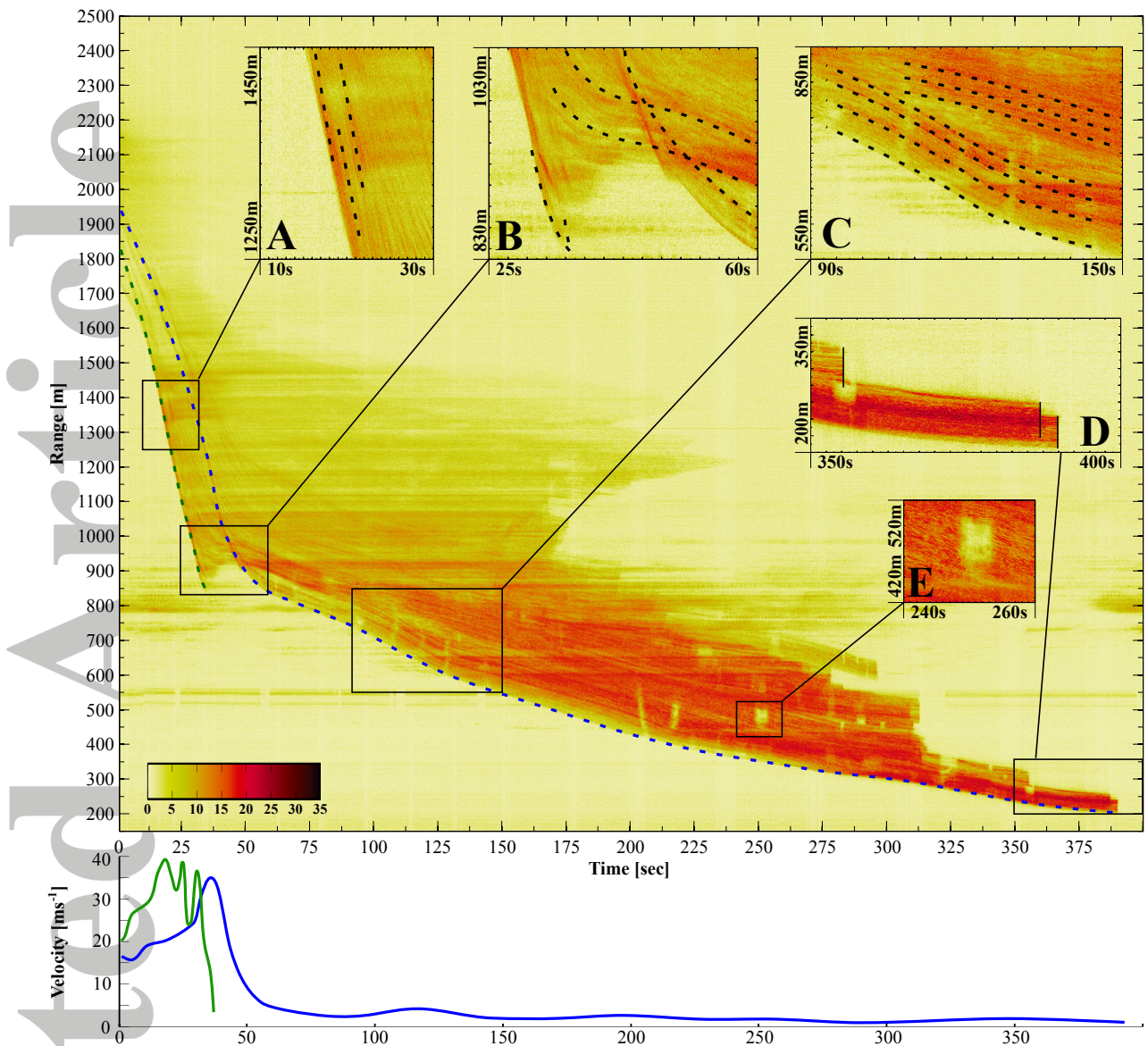
Figure 8. Avalanche #13-3019 naturally released on 1 of February 2013 from Crêta Besse 1/2. This avalanche is a typical example of transitional flow characterised by cold regimes in the upper part of the flow and a transition to the warm plug regime (WPR) starting from 900 m range. This range approximately corresponds to the snowfall limit, below which the rain wetted the snow cover. The first front starves at the end of the couloir, but the second front turns into the WPR and continues until the valley floor.
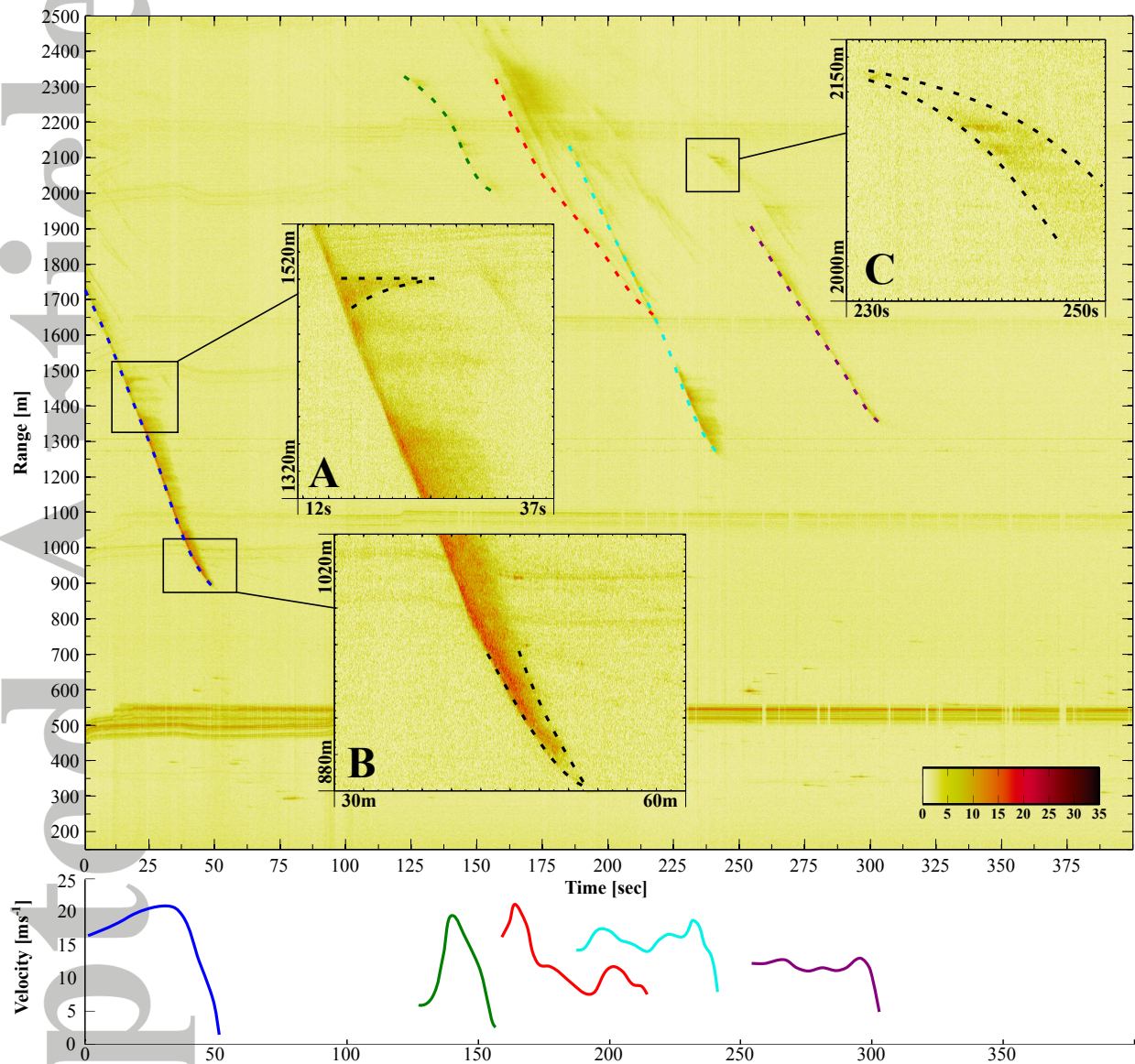
Figure 9. Multiple small avalanches occurred on 6 December 2012 between Crêta Besse 1 and 2 (#13-3005). These avalanches are typical examples of the cold dense regime. They have a remarkably short flowing length of only around 100 m and they are characterised by a single surge.
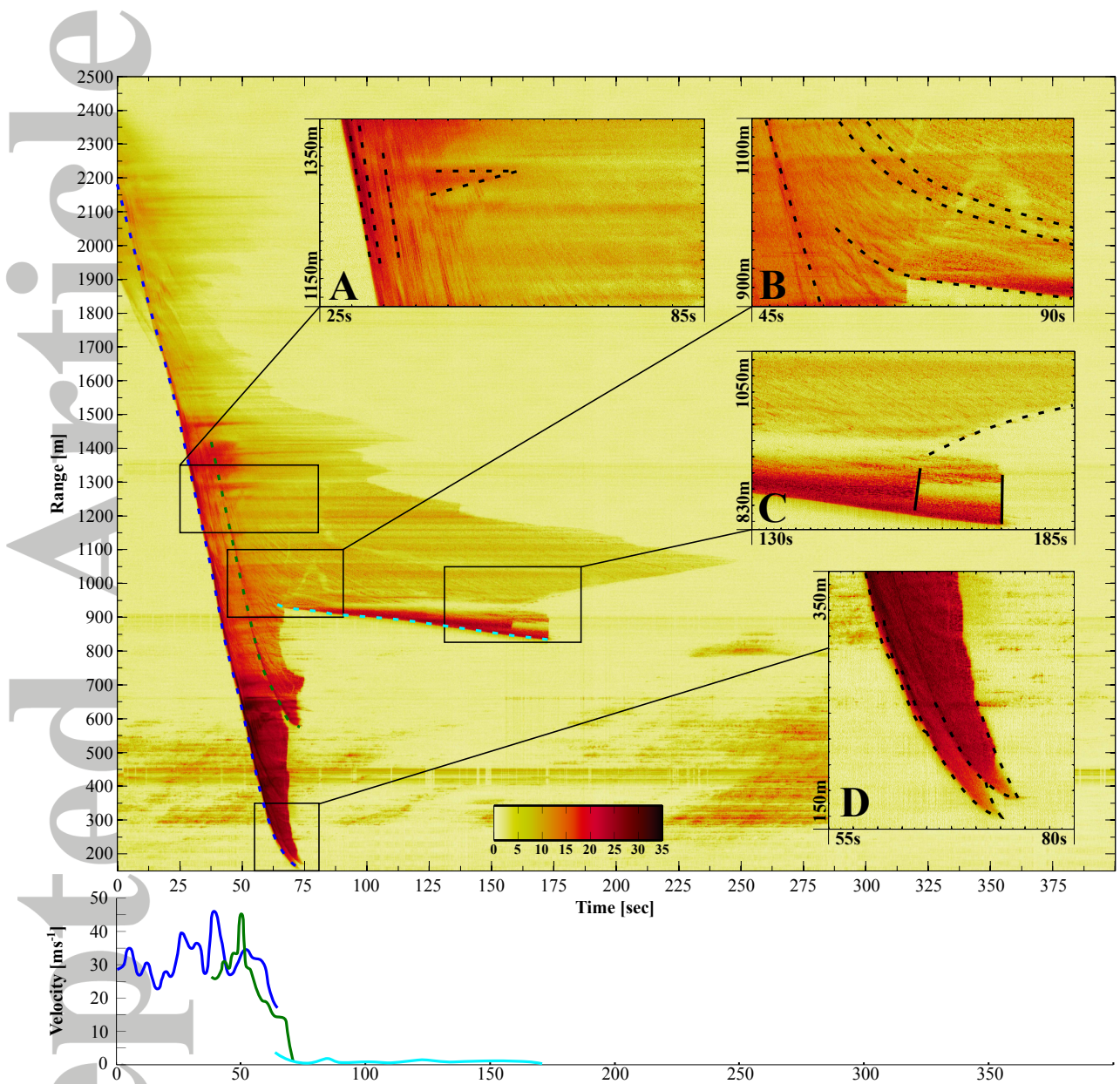
Figure 10. A fully developed powder snow avalanche #14-0012 occurred on 13 February 2014 from Crêta Besse 1. The avalanche is characterised by up to six different flow regimes, indicating a complex interplay between cold and warm snow.